Glial activation and central synapse loss, but not motoneuron degeneration, are prevented by the sigma-1 receptor agonist PRE-084 in the *Smn*$^{2B/-}$ mouse model of spinal muscular atrophy

Clàudia Cerveró[1], Alba Blasco[1], Olga Tarabal[1], Anna Casanovas[1], Lídia Piedrafita[1], Xavier Navarro[2], Josep E. Esquerda[1], and Jordi Calderó[1,*]

[1]Unitat de Neurobiologia Cel·lular, Departament de Medicina Experimental, Facultat de Medicina, Universitat de Lleida and Institut de Recerca Biomèdica de Lleida (IRBLLEIDA), Av. Rovira Roure 80, 25198 Lleida, Catalonia, Spain

[2]Group of Neuroplasticity and Regeneration, Institute of Neurosciences and Department of Cell Biology, Physiology and Immunology, Universitat Autònoma de Barcelona and CIBERNED, 08193, Bellaterra, Catalonia, Spain

Running title: Chronic PRE-084 treatment in SMA

Original research article

*Corresponding author: Jordi Calderó, Unitat de Neurobiologia Cel·lular, Departament de Medicina Experimental, Facultat de Medicina, IRBLLEIDA, Universitat de Lleida, Av. Rovira Roure 80, 25198 Lleida, Catalonia, Spain.

Phone: +34-973-702440

E-mail address: jordi.caldero@mex.udl.cat

This work was supported by grants from the *Ministerio de Economía y Competitividad* co-financed by FEDER (SAF2015-70801).

Author contributions: J.C., J.E.E. and X.N. conceived and designed the experiments. C.C., A.B., A.C., L.P., and O.T. performed the experiments. C.C., A.B., and J.C. analyzed the data. J.C., J.E.E. and C.C. wrote the paper.

The authors declare that no conflict of interest exists.

ABSTRACT

Spinal muscular atrophy (SMA) is characterized by the loss of α-motoneurons (MNs) with concomitant muscle denervation. However, not all MNs are equally susceptible to degeneration in MN diseases, including SMA. This differential vulnerability has been linked to MN excitability, which can be modulated by cholinergic inputs via C-type synaptic boutons. Sigma-1 receptor (Sig1R) is expressed in MNs and particularly enriched in C-boutons. Alterations in Sig1R have been associated with MN degeneration. Here, we investigated whether a chronic treatment with the Sig1R agonist PRE-084 was able to exert beneficial effects on SMA. We used a model of intermediate SMA, the *Smn*$^{2B/-}$ mouse, in which we performed a detailed characterization of the histopathological changes that occur throughout the disease. We report that *Smn*$^{2B/-}$ mice exhibited qualitative differences in major alterations found in mouse models of severe SMA. In this respect, *Smn*$^{2B/-}$ animals exhibited more prominent MN degeneration with early motor axon alterations, marked changes in sensory neurons, and later MN deafferentation which correlated with conspicuous reactive gliosis and altered, neuroinflammatory, M1/M2 microglial balance. PRE-084 treatment attenuated reactive gliosis, mitigated M1/M2 imbalance and prevented MN deafferentation in *Smn*$^{2B/-}$ mice. These effects can also be observed in a severe SMA model, the SMNΔ7 mouse. However, the prevention of gliosis and MN deafferentation promoted by PRE-084 were not accompanied by any improvements in clinical outcome or other major pathological changes found in SMA mice.

Key words: spinal muscular atrophy; *Smn*$^{2B/-}$ mouse; SMNΔ7 mouse; sigma-1 receptor; C-boutons; microglia; motoneuron synaptic afferents

INTRODUCTION

Spinal muscular atrophy (SMA) is a genetic, autosomal recessive, neuromuscular disorder predominantly characterized by a progressive loss of α-motoneurons (MNs), atrophy of skeletal muscles and motor impairment (1). With an incidence of 1 in 6,000-10,000 live births and a carrier frequency of 1 in 35-50 (2, 3), this disease is the leading genetic cause of infant mortality. SMA is caused by deletion or inactivating mutations of the *survival motor neuron 1* (*SMN1*) gene located in the telomeric position of chromosome 5q13 (4). *SMN1* is ubiquitously expressed and plays an important role in mRNA splicing by orchestrating small nuclear ribonuclear protein complex assembly (5). Humans possess an almost identical copy of *SMN1*, referred to as *SMN2;* which is also located on chromosome 5, but in its centromeric region. *SMN2* differs from *SMN1* in terms of an exon 7 C-to-T transition. This change alters the normal splicing of mRNA and leads to the production of ~85-90% *SMN2* transcripts that lack exon 7. When these transcripts are traduced, a truncated and unstable protein (SMNΔ7) is produced (6), resulting in inefficient levels of functional, full-length (FL), SMN protein. Depending on the age of onset and the severity of disease, SMA can be clinically classified into several different types; these range from type I (the severest form) to type IV (the mildest form). The severity of the disease is inversely correlated with the *SMN2* copy number (7, 8). Thus, the most severely affected patients are usually the ones with the fewest copies of *SMN2*.

Since the identification of the loss-of-function defects in *SMN1* gene as the cause of SMA, intensive efforts have been made to develop experimental therapeutic approaches to increase SMN protein (see for reviews (9-12)). Small molecules, such as antisense oligonucleotides (ASOs), which promote *SMN2* exon 7 inclusion and thereby increase FL *SMN2* transcription, and viral gene therapies, which directly replace *SMN1,* are

promising strategies for SMA. In this regard, the ASO Nusinersen, which acts as a splicing modifier targeting the intronic splicing silencer N1 in *SMN2* intron 7 (13), has been recently approved for SMA treatment. Clinical trials have shown that Nusinersen administration results in a significant improvement in motor function and survival of type I SMA infants (14-17). Even so, there is still a need for complementary, SMN-independent, approaches which target cellular and molecular elements that are disturbed by the SMN deficiency. These therapies, used in synergy with SMN-targeted strategies, appear to be important for the long-term preservation of the neuromuscular structure and function (12).

The reason why insufficient levels of SMN protein predominantly lead to MN loss is still unclear (18). Moreover, it is known that, in the case of MN diseases, not all MNs exhibit a similar susceptibility to degeneration: while some MNs degenerate early, others remain apparently undamaged until the end-stages. This differential vulnerability of different MN subtypes appears to be related to their excitability (19). The highly organized pattern of MN activity and excitability is modulated by cholinergic inputs delivered through C-type synaptic boutons. C-boutons may therefore be ultimately related to MN susceptibility to degeneration (20, 21).

C-boutons exhibit a highly specialized postsynaptic organelle known as subsurface cistern (SSC), which is closely related to the endoplasmic reticulum (ER) lamellae and adjacent to the postsynaptic membrane (22). The molecular organization of C-boutons includes: M2 muscarinic receptors (23), voltage-gated K^+ channels (Kv2.1) and Ca^{2+}-activated K^+ channels (SK) (24, 25), sigma-1 receptors (Sig1Rs) (26), and neuregulin-1 (NRG-1) (27). All of these molecules seem to be clustered together in specific microdomains. However, the role of some of them, including Sig1R and NRG-1, in C-bouton regulation still remains unknown.

The Sig1R is a transmembrane protein with chaperone-like activity, which is widely distributed in mammalian central and peripheral nervous systems. This protein is mainly located in the ER. Sig1R is particularly enriched in a sub-region of the ER in which their cisternae come into contact with mitochondria; this point of contact is known as the mitochondrion-associated ER membrane (MAM) (28). Sig1R, which acts as an inter-organelle signaling modulator, is involved in several cellular processes which include the regulation of ER-mitochondrion signaling and ER-nucleus crosstalk (29). Sig1R also appears to play a role in unfolded protein response control and in the protection of cells from both oxidative and ER-mediated cellular stress (30). Following ligand stimulation, Sig1R can also translocate from the MAM to other parts of the cell. Sig1R can therefore interact with several different ion channels, receptors and/or kinases in the plasma membrane (31). In neurons, Sig1R mediates the regulation of several different processes, such as neuritogenesis, K^+ channel and N-methyl-D-aspartate (NMDA) receptor activity and Ca^{2+} homeostasis (31-33). Sig1R stimulation has also been shown to modulate multiple aspects of microglial activity (34-36). Mutations of the *Sig1R* gene are related to MN disorders, such as amyotrophic lateral sclerosis (ALS) (37, 38). Moreover, a lack of Sig1R exacerbates ALS progression in a mouse model of the disease (39). The synthetic Sig1R agonist 2-(4-morpholinethyl)1-phenylcyclohexanecarboxylate (PRE-084) has been reported to confer neuroprotection after excitotoxic stimuli *in vitro* (40) and after spinal root avulsion in rats (34). Furthermore, the administration of PRE-084 in the $SOD1^{G93A}$ mouse model extends survival and improves motor function by preventing MN death and preserving neuromuscular connections (41). More recently, the neuroprotective effects of PRE-084 in a mouse model of MN disease not linked to SOD mutation have also been described (42).

In the present study we wanted to investigate whether chronic treatment with PRE-084 was able to elicit beneficial effects on SMA. To check this, we used the *Smn*$^{2B/-}$ mouse, a model for intermediate SMA (43, 44), whose lifespan is prolonged until about 25-30 days and in which the phenotypic features of disease are more gradual than in murine models for severe SMA (e.g. *Smn*$^{-/-}$;*SMN2*$^{+/+}$ or SMNΔ7 mice). We started by examining the progression of pathological changes in the spinal cord, dorsal root ganglion, motor and sensory nerves, and neuromuscular junctions (NMJs) of *Smn*$^{2B/-}$ mice throughout the disease. These changes were correlated with motor disabilities in mice. Here, we show that, in comparison with severe SMA mouse models, the *Smn*$^{2B/-}$ mouse exhibited substantial differences in the degree and time-course of MN degeneration and deafferentation. We also report that the PRE-084 treatment in *Smn*$^{2B/-}$ robustly prevented reactive gliosis in the spinal cord and restored the altered microglial phenotypic (M1/M2) balance associated with SMA. This effect of PRE-084 mitigating gliosis was also reproduced in SMNΔ7 mice. Although PRE-084 partially prevented the loss of afferent inputs to MNs linked to SMA, it was, however, unable to prevent MN degeneration. PRE-084 was also able to improve neurofilament (NF) accumulation in motor nerve terminals, but failed to ameliorate other major pathological changes found at the neuromuscular junctions (NMJs) in SMA mice. Furthermore, no improvement in survival or motor abilities was observed in SMA animals treated with PRE-084.

MATERIALS AND METHODS

Mice and pharmacological experiments with PRE-084

The SMNΔ7 and *Smn*$^{2B/-}$ mouse lines were used. To generate SMNΔ7 animals, *Smn*$^{+/-}$;*SMN2*$^{+/+}$;*SMNΔ7*$^{+/+}$ mice (heterozygote knockouts for the *Smn* gene, FVB.Cg-

Tg[SMN2*delta7]4299Ahmb Tg[SMN2]89Ahmb Smn1tm1Msd/J, stock number 005025) were purchased from The Jackson Laboratory (Sacramento, CA, USA); heterozygous female and male animals were crossed to obtain *Smn*$^{-/-}$*;SMN2*$^{+/+}$*;SMNΔ7*$^{+/+}$ (homozygote knockouts for the *Smn* gene, referred as SMNΔ7) and *Smn*$^{+/+}$*;SMN2*$^{+/+}$*;SMNΔ7*$^{+/+}$ (wild-type for the *Smn* gene, hereafter referred as WT) mice.

The *Smn*$^{2B/-}$ mice (C57BL/6 background) were obtained by crossing heterozygote knockout for the *Smn* gene (*Smn*$^{+/-}$ [B6.Cg-Smn1^{tm2Mrph}/J, stock 007963], The Jackson Laboratory) males with homozygote for the 2B mutation (*Smn*$^{2B/2B}$) females, which were a kind gift from Dr Rashmi Kothary (University of Ottawa, Canada). The 2B mutation consists of a substitution of three nucleotides in the exon splicing enhancer of exon 7 (45). *Smn*$^{2B/+}$ heterozygous mice do not exhibit any apparent SMA phenotype (46) and were therefore used as controls (hereafter referred to as WT).

SMNΔ7 mice exhibit a severe postnatal SMA phenotype, with overt symptomatology and pathological changes in the spinal cord and skeletal muscles at 7-8 days after birth, and have a mean lifespan of about 2 weeks (47-50). *Smn*$^{2B/-}$ animals develop a milder postnatal SMA phenotype, with a lower growth-related gain in body weight from about postnatal day (P) 12, and neuromuscular histopathological alterations and motor function deficits at about P16-17; *Smn*$^{2B/-}$ animals have a mean lifespan of about 3-4 weeks ((46, 51) and our own observations).

At P0, a piece of tail was removed from the mice for subsequent genotyping. The REDExtract-N-Amp Tissue PCR Kit (Sigma, St Louis, MO) was used for genomic DNA extraction and polymerase chain reaction setup. To distinguish between SMNΔ7 mice and their WT littermates, the following primers were used: WT forward 5' ctccgggatattgggattg 3', SMNΔ7 reverse 5' ggtaacgccagggttttcc 3' and WT reverse 5'

tttcttctggctgtgccttt 3'. To identify *Smn*$^{2B/-}$ mice, the gene that had to be detected was lacZ; this was used to interrupt the *Smn* murine gene (52). The primers used were: lacZ forward 5' ttggcctgaactgccagctggcgcagg 3' and lacZ reverse 5'tcccgcagcgcagaccgttttcgctcg 3'. Electrophoresis in 1.5% agarose gel and SYBR safe DNA stain (Molecular Probes, Eugene, OR) was run at 100 V.

WT and SMA (SMNΔ7 or *Smn*$^{2B/-}$) mice were treated with either PRE-084 (Tocris Bioscience, Bristol, United Kingdom; 0.25 mg/Kg/day) or the corresponding volume of physiological saline solution (vehicle). The PRE-084, or vehicle, was administered once a day, in the morning from P1 until the end of the experimental time frame, via subcutaneous interscapular injections. The dosage, regimen and mode of PRE-084 administration used here were similar to those used in previous studies (41, 42). At selected points in time, the mice were anaesthetized with an intraperitoneal injection of pentobarbital (2%, 1 ml/10 g body weight), and transcardially perfused with physiological saline solution, followed by 4% paraformaldehyde (PFA) in 0.1 M phosphate buffer (PB) at pH 7.4. Mice used for electron microscopy studies were perfused with a solution containing 1% PFA and 1% glutaraldehyde in 0.1 M PB at pH 7.4. Tissue samples were rapidly dissected, removed, and subsequently processed as indicated below. All the experimental procedures were carried out according to the guidelines of the committee for Animal Care and Use of the University of Lleida, which have been approved by the *Generalitat de Catalunya*.

Behavioral phenotype testing

To evaluate disease progression, the mice were weighed every morning and carefully examined in order to detect the presence of any specific signs and/or symptoms of disease. Thereafter, the righting reflex and hind-limb suspension test ("tube test") were

conducted to assess the motor abilities of the SMNΔ7 mice from P0-1 until their death, and *Smn*$^{2B/-}$ mice from P0-1 to P10. These tests were scored following the guidelines described elsewhere (50, 53).

From P10, the motor behavior of *Smn*$^{2B/-}$ mice was assessed by performing tests to analyze their motor balance and muscular strength: pen test and grip test. For the pen test, mice were placed on a suspended rope, as previously described (54). The latency to fall and the number of hindlimbs that mice were capable of grasping on the rope (2, 1 or 0) were measured. For the grip test, mice were placed on a surface whose slope was progressively increased; we noted the maximum slope that the mice were able to remain on for a period of 20 seconds without falling (55).

Tests were conducted by the same investigator (who was blind to the experimental condition). In each test, each individual mouse was examined three times, with a 15-minute recovery period between tests. The average values from the three independent tests were then determined in order to obtain the final score.

Muscle and spinal cord histology and MN counts

Tibialis anterior (TA) and intercostal (IC) muscles, and spinal cords were rapidly dissected and removed for subsequent histological analysis and MN counting.

Muscles were weighed, postfixed in 4% PFA in 0.1 M PB (pH 7.4), cryoprotected with 30% sucrose in 0.1 M in PB, embedded in Tissue Freezing Medium (TFM, Triangle Biomedical Sciences, Durham, NC, USA), and then frozen. Multiple cryostat transverse sections (16-µm thick) were obtained from the mid-belly of the muscle. Sections were subsequently stained with hematoxylin and eosin (H&E).

For MN counts, spinal cords were fixed in Bouin's solution and embedded in paraffin. Serial transverse sections (14-µm thick), obtained throughout the entire lumbar

segment, were stained with H&E. Apparently healthy MNs present in the ventral horn were identified by their size and shape and counted blindly on one side of every 10th section, following previously described procedures (56, 57). Briefly stated, only MNs with a large nucleus, a visible clump of nuclear material and a substantial cytoplasm were counted. The total number of MNs per ventral horn was obtained by multiplying the number of cells counted by 10.

Immunocytochemistry and imaging

For immunocytochemical studies, TA and IC muscles, lumbar spinal cords and L4 dorsal root ganglia (DRGs) were postfixed by immersion in 4% paraformaldehyde in 0.1 M PB, at pH 7.4, either for 2 hours (in the case of muscles) or overnight (in the case of spinal cords and DRGs), and then cryoprotected. Tissue samples were embedded in TFM and frozen. Longitudinal (for muscles, 16-µm thick) and transverse (for spinal cords and DRGs, 14-µm thick) serial cryostat sections were obtained and then stored at -80ºC.

Sections were sequentially rinsed for 30 minutes in phosphate-buffered saline (PBS) containing 0.1% Triton X-100, then blocked in normal goat serum or normal horse serum, and subsequently incubated overnight with the chosen primary antibody. The following primary antibodies were used: goat polyclonal anti-matrix metalloproteinase-9 (MMP-9; diluted 1:10; Sigma-Aldrich, Madrid, Spain; catalog no. M9570) rabbit polyclonal anti-ionized calcium-binding adaptor molecule 1 (IBA1, diluted 1:500; Wako Pure Chemical Industries Ltd., Osaka, Japan; catalog no. 019-19741); chicken polyclonal anti-glial fibrillary acidic protein (GFAP, diluted 1:1000; Abcam, Cambridge, UK; catalog no. Ab4674); chicken polyclonal anti-neurofilament 68 KDa (NF, diluted 1:1000; Abcam; catalog no. ab72997); mouse monoclonal anti-synaptic vesicle protein 2 (SV2; diluted 1:1000; Developmental Studies Hybridoma Bank

[DSHB], Iowa City, IA; catalog no. SV2); rat monoclonal anti-Mac-2 (diluted 1:800; Cedarlane, Burlington, Canada; catalog no. CL8942AP); goat polyclonal anti-CD206 (diluted 1:100; RD Systems, Minneapolis, MN; catalog no. AF2535); rabbit polyclonal anti-NRG1 (diluted 1:100; Santa Cruz; catalog no. sc-348); mouse monoclonal anti-Sig1R (diluted 1:50; Santa Cruz; catalog no. sc-137075); guinea pig polyclonal anti-vesicular acetylcholine transporter (VAChT, diluted 1:300; Synaptic Systems, Goettingen, Germany; catalog no. 139105); guinea pig polyclonal anti-vesicular glutamate transporter 1 (VGluT1, diluted 1:500; Synaptic Systems; catalog no. 135304); guinea pig polyclonal anti-vesicular GABA transporter (VGAT, diluted 1:200; Synaptic Systems; catalog no. 131004); rabbit polyclonal anti-NMDA NR1 subunit (NR1, diluted 1:250; Abcam; catalog no. ab17345); rabbit polyclonal anti-phospho NR1 (Ser897) (p-NR1, diluted 1:500; Millipore; catalog no. ABN99); rabbit polyclonal anti-calcitonin gene-related peptide (CGRP, diluted 1:1000; Sigma-Aldrich; catalog no. C8198); and mouse monoclonal anti-parvalbumin (PV, diluted 1:5000, Swant, Marly, Switzerland; catalog no. PV 235).

After incubation with the primary antibody, the sections were washed and then incubated at room temperature (RT) for 1 hour with the appropriate secondary fluorescent antibodies: DyLight 488-conjugated donkey anti-rabbit IgG; DyLight 549-conjugated donkey anti-rat or anti-chicken IgG; DyLight 649-conjugated donkey anti-mouse or anti-chicken IgG; Cy3-conjugated donkey anti-rabbit, anti-mouse or anti-goat IgG (all diluted 1:500, from Jackson ImmunoResearch Laboratories, West Grove, PA); and Alexa Fluor 488-conjugated goat anti-chicken IgG and Alexa Fluor 647-conjugated donkey anti-guinea pig IgG (diluted 1:500; Molecular Probes). Sections were also stained with 4’,6-diamidino-2-phenylindole dihydrochloride (DAPI, 50 ng/ml, Molecular Probes) for DNA labeling. Muscle sections were also incubated with Alexa

Fluor 488-conjugated α-bungarotoxin (α-Bgtx, diluted 1:500; Molecular Probes) to identify postsynaptic acetylcholine receptors. Spinal cord sections were counterstained with NeuroTrace 530/615 red or NeuroTrace 435/455 blue fluorescent Nissl stain (Molecular Probes). Some slides with DRG sections were stained with the FITC-conjugated *Bandeiraea simplicifolia* lectin (isolectin B_4, IB4, diluted 1:25; Sigma-Aldrich). After washing, slides were coverslipped using Vectashield (Vector Laboratories, Burlingame, CA) or Mowiol (Calbiochem, San Diego, CA). Slides were examined with an Olympus BX51 epifluorescence microscope (Olympus, Hamburg, Germany) equipped with a DP30BW camera or FluoView 500 or FluoView 1000 Olympus laser scanning confocal microscopes. For comparisons, slides from different animals and experimental conditions were processed in parallel for immunocytochemistry and subsequent imaging. The same scanning parameters were used for the acquisition of images corresponding to different experimental groups. For spinal cord immunocytochemical studies, digital images of the entire lumbar region were obtained from every 30th section.

Electron microscopy

Ventral and dorsal nerve roots (VRs and DRs, respectively) were separately dissected, postfixed in 1% osmium tetroxide, and embedded in EMbed 812 (Electron Microscopy Sciences, Fort Washington, PA) epoxy resin, following standard procedures. Semithin sections (1-μm thick) stained with methylene blue were examined and imaged using an Olympus 60X/1.4 NA PlanApo oil immersion objective (Olympus, Hamburg, Germany) and a DMX 1200 Nikon (Tokyo, Japan) digital camera. Ultrathin sections were counterstained with uranyl acetate and lead citrate and then observed in a Zeiss EM 910 (Zeiss, Oberkochen, Germany) electron microscope.

Image and morphometric analysis

The cytoarchitecture of the NMJs was analyzed in longitudinal immunostained sections of muscle. Z-stack optical sections (1 μm-thick) were obtained and projected to reconstruct NMJs using microscope software. Five to nine sections were analyzed for each muscle and animal, and 50-75 NMJs from randomly selected visual fields were evaluated for each experimental condition. NMJ size was assessed by determining the area of the α-Bgtx-labeled postsynaptic site, which was manually outlined using ImageJ software (National Institutes of Health, USA). A NMJ was considered to be denervated when the percentage of α-Bgtx-labeled postsynaptic surface covered by the SV2-stained presynaptic terminal was less than 15% (50, 58). Based on the structural appearance of each postsynaptic site, the degree of NMJ maturity was classified as: plaque, folds, perforations, or secondary structure (pretzel-like morphology), with this ranging from immature to mature, according to previously described criteria (50, 58). NF was considered to accumulate in the presynaptic sites when the terminal portion of axons exhibited a swollen morphology and was strongly stained with the anti-NF antibody. Any NMJs that were difficult to analyze due to their location and/or orientation were excluded from the analysis.

Levels of GFAP and IBA1 immunoreactivitity in the spinal cord were quantified by digital image analysis using ImageJ software. The number of NRG-1- and Sig1R-immunolabeled profiles, and VAChT, VGluT1 and VGAT immunoreactive synaptic boutons on MN somata was counted on the screen; only boutons that were in close contact with MNs exhibiting a large nucleus, visible nucleolus and healthy appearance were included in these counts; the numbers were then normalized to the perimeter of MN soma.

The number and soma area of CGRP, IB4 and PV immunopositive sensory neurons in the DRGs were measured using digital images taken from cryostat sections and ImageJ software. The area of DRG neurons was also assessed in sections counterstained with NeuroTrace fluorescent Nissl stain (Molecular Probes).

Axon diameter and *g*-ratio measurements were performed on electron micrographs of VRs and DRs taken from mice at different points in time. For *g*-ratio analysis, we used the ImageJ *g*-ratio plug-in; this allowed us to obtain semiautomated measurements of randomly selected nerve fibers. The axon diameter was divided by the outer diameter of the myelin sheath. At least 100 myelinated axons per mouse (3 mice per condition) were measured. The number and diameter of healthy and degenerating myelinated axons was determined from 60X images taken from VR and DR cross semithin sections stained with methylene blue. The images were joined together to obtain a whole picture of a complete nerve root transverse section. The diameter of the myelinated axons was measured by delineating the outer profile of the myelin sheath.

Western blotting

Frozen spinal cords were fragmented and homogenized with blending buffer 1 x SR (2% SDS and 125 mM Tris-HCl, pH 6.8) supplemented with protease inhibitor (Sigma, Ref. P8340) and PhosSTOP (Roche, Laval, Canada). The homogenized samples were then heated to 100 ºC for 5 minutes and centrifuged at 12,000 rpm for 5 minutes. The protein concentrations of supernatants were determined by BIO-RAD Micro DC protein assay (BIO-RAD, Laboratories Inc., Hercules, CA, USA). Loading buffer 4 x SS (20% sucrose and 0.05% bromophenol blue, 0.1% sodium azide) containing 5-10% β-mercaptoethanol (Sigma) and 15 µg of protein was then loaded into a 10% or 15% polyacrylamide electrophoresis gel. Proteins were electrotransferred to PVDF (ImmobilonTM-P, Millipore, Bredford, MA, USA) membranes in a Tris-glycine-

methanol-buffered solution. The membranes were then blocked with 5% dried skimmed milk in 0.1% Tween 20 and Tris-buffered saline pH 8 (TBST) for 1 hour at RT, and then extensively washed in TBST. Immunodetection was performed by incubating the membranes overnight at 4ºC with the following antibodies: rabbit polyclonal anti-NR1 (diluted 1:250; Abcam); rabbit polyclonal anti-p-NR1 (Ser897, diluted 1:500; Millipore); mouse monoclonal anti-SMN (diluted 1:1000; BD Biosciences, San Jose, CA, USA; catalog no. 610647); mouse monoclonal anti-β-actin (diluted 1:1000; Sigma; catalog no. A54441). The antibody against β-actin was used for loading controls. The membranes were washed in TBST, incubated for 60 min at RT with the appropriate peroxidase-conjugated secondary antibodies (1:5000; Amersham Biosciences, Buckinghamshire, UK), washed in TBST, and visualized using the ECL Prime Western Blotting Detection Reagent detection kit (GE Healthcare, Buckinghamshire, UK), following the procedure described by the manufacturer. The quantification of band densities was performed by using Chemi-Doc MP Imaging System (BIO-RAD Laboratories Inc.).

Statistical analysis

Data were expressed as means ± SEM. The statistical analysis was assessed by either one- or two-way analysis of variance (ANOVA) followed by post-hoc Bonferroni's multiple comparison test or Student's *t*-test when only two different groups were compared. Differences were considered to be statistically significant if $p \leq 0.05$.

RESULTS

Behavioral alterations, MN loss and motor axon degeneration in *Smn*$^{2B/-}$ mice

With the progression of disease, SMA mice exhibit less body-weight gain than their WT littermates and suffer gradual impairment of their motor performance, as reported for different types of murine models (48). *Smn*$^{2B/-}$ mice develop a milder form of the disease, with phenotypic changes and motor deficits occurring more gradually than in other extensively used SMA mouse models (51). In line with previous reports (59), in *Smn*$^{2B/-}$ animals, we did not find any significant reduction in body weight or any apparent alterations in motor abilities until P12-14, with a mean lifespan of about 28 days (not shown). The changes in motor performance and survival in *Smn*$^{2B/-}$ mice observed in our study during the progression of disease are shown in supplementary Fig. 1a-e.

We first characterized the time of onset and the degree of MN death during the course of disease in the *Smn*$^{2B/-}$ mice. Apparently healthy MNs were counted on H&E-stained transverse serial sections of the entire, paraffin-embedded, spinal cord lumbar segment, according to established criteria (56, 57). In contrast to the moderate MN loss found in the lumbar spinal cord of different mouse models of severe SMA (i.e. *Smn*$^{+/-}$ *;SMN2*$^{+/+}$ or SMNΔ7 mice (49, 60)), *Smn*$^{2B/-}$ animals undergo progressive and prominent MN degeneration (Fig. 1A). In this model, a depletion of MNs had already been observed at P5, but was even more marked and significant at P10 (~30% of WT mice). Interestingly, and as mentioned above, at none of these ages did we detect any perceptible alterations in motor behavior in diseased animals. A still more dramatic fall in the number of MNs was seen at P20 (~75% of WT animals), followed by only a minor additional MN loss during the end-stage of disease (from P20 to P25-30). *Smn*$^{2B/-}$ MNs also displayed a significant size reduction, which had already been noticeable at P5; this became particularly marked at P10 (~55% of WT MNs), but then barely changed from P10 to P25-30 (Fig. 1B). The appearance of MNs in the lumbar spinal

cord of WT and *Smn*$^{2B/-}$ mice is shown in Fig.1C-G. In diseased animals, the scarce MNs which remained in the ventral horn at end-stages displayed an abnormal morphology compatible with ongoing cell degeneration. Some of these degenerating MNs appeared surrounded of nuclear profiles which probably correspond to microglia recruited by the sick cell (Fig. 1G).

Several studies have reported the differential vulnerability of spinal MNs to degeneration in ALS (61, 62). MNs innervating slow-twitch muscles (slow MNs) are therefore more resistant than those innervating fast-twitch muscles (fast MNs). In particular, fast-fatigable MNs are the ones most severely affected and which degenerate earliest during disease; they are followed by fast-fatigue resistant and slow MNs, which persist until later stages of disease. To determine whether the vulnerability of fast MNs is also a feature of SMA, we performed an immunocytochemical analysis of MMP-9 expression in the lumbar spinal cord of WT and *Smn*$^{2B/-}$ mice. MMP-9 has been shown to be selectively expressed in fast MNs prior to the onset of ALS disease in SOD1 mice (63). We did not find any signs of MMP-9 immunoreactivity in the spinal MNs of either WT or diseased animals at P1. However, as shown in Fig. 1H and I-N', at P5 ~58% of WT MNs exhibited MMP-9 positive immunolabeling, whereas this was observed in ~40% of the surviving *Smn*$^{2B/-}$ MNs (~18% reduction *vs.* WT, $p<0.05$). The percentage of MNs showing MMP-9 expression then fell to ~17% in *Smn*$^{2B/-}$ mice at P20 (~48% reduction *vs.* P20 WT, $p<0.001$). Taking into account the fact that *Smn*$^{2B/-}$ mice showed ~16% fewer MNs than age-matched WT littermates at P5, overall, these results suggest a preferential loss of fast-fatigable MNs during the early stages (P5) of disease in the *Smn*$^{2B/-}$ mice; the degeneration this MN subtype progresses until end-stages of SMA.

It has been hypothesized that MN death in SMA is a consequence of a retrograde "dying-back" degeneration of motor axons which occurs at postnatal ages (64). This

would imply that pathological changes would start in the distal part of the motor axons and/or NMJs, and progress to MN cell bodies. To explore whether or not axonal alterations preceded MN death, L4 VRs taken from WT and *Smn*$^{2B/-}$ mice at different ages were embedded in plastic resin and then transversal sections were examined after methylene blue staining. As shown in Fig. 2A, the VRs from WT animals exhibited a progressive increase in myelinated axon diameter (including the myelin sheath) during the whole postnatal period; this reflected the maturation process of the motor nerves. In contrast, in the VRs of *Smn*$^{2B/-}$ mice, this normal axonal growth was significantly reduced at P25-30 (Fig. 2A and B). At all the time points studied, VRs from diseased mice contained fewer healthy myelinated axons than those from WT littermates (not shown). Moreover, a significant increase in the number of degenerating axons was observed in the VRs of *Smn*$^{2B/-}$ mice from P20 onwards (Fig. 2C-K). Interestingly, we noticed that at P5 about 5% of the myelinated axons in *Smn*$^{2B/-}$ VRs exhibited spheroidal masses resembling myelin ball structures, which were hardly ever seen in WT VRs (Fig. 2L and M). The ultrastructural analysis of VRs at P5 revealed that the vast majority of axons in WT animals exhibited a normal appearance Fig. 3A,B). We only occasionally found some axons in WT VRs that showed structural regressive abnormalities (Fig. 3B); this was probably the result of a physiological remodeling process taking place in the motor nervous system during the early postnatal period of development (65-68). Conversely, a significant number of motor axons in *Smn*$^{2B/-}$ animals exhibited inclusions in the form of myelin-like multilaminar structures similar to those observed during Wallerian degeneration; in some cases, such myelin debris had been engulfed by phagocytic cells (Fig. 3C-F). Additionally, the axon diameter, determined by delineating the axon periphery under the myelin sheath, was found to be significantly longer in the VRs of *Smn*$^{2B/-}$ mice than in those of their WT littermates; this would seem

to indicate the presence of motor axon swelling in the SMA (Fig. 3G). Conversely, the myelin in motor axons of diseased animals was significantly thinner (*g*-ratio: 0.69 ± 0.01, n = 100-125 per animal) than that in motor axons of WT mice (*g*-ratio: 0.63 ± 0.01, n = 100-123 per animal) (Fig. 3H). Fig. 3I shows a scatter plot displaying *g*-ratios as a function of axon diameter: all of the axons in VRs from diseased animals showing higher size corresponded to those with higher *g*-ratios (implying thinner myelin). On the other hand, the Schwann cells enwrapping axons in healthy animals appeared to be more mature than those observed around degenerating axons in $Smn^{2B/-}$ mice (Fig. 3A and D-F). Overall, these data point to the expected existence of progressive atrophy and degeneration of motor axons as SMA progresses. Although in SMA animals this motor axon degeneration is not statistically significant until P20 (coinciding with both prominent MN loss and marked motor disabilities), axonal morphological alterations are already present at P5; these alterations include: swelling, hypomyelination and Wallerian-like degeneration, and correlate with the incipient MN death found at the same time point of disease.

Changes in DRG cells and DR axons in $Smn^{2B/-}$ mice

Sensory defects have been reported to occur in humans in the most severe forms of SMA (type I), but not in type II or III SMA (69-71). It has been shown that DRG sensory neurons are also affected in $Smn^{-/-}$;*SMN2* mice, which are a model for human type I SMA (72). To explore whether DRG neurons of $Smn^{2B/-}$ mice also displayed pathological changes, L4 DRGs from WT and SMA mice were taken at P20, an age at which, as previously mentioned, we had observed massive MN degeneration. DRG cryostat sections were processed for immunocytochemistry using antibodies against CGRP and PV, and stained with IB4, as specific markers for different neuronal subpopulations: CGRP is present in peptidergic sensory nociceptive neurons, which are

small and unmyelinated; IB4 exclusively stains non-peptidergic sensory nociceptive neurons, which are small and unmyelinated; and PV is localized in large sensory proprioceptive neurons that innervate muscle spindles (73-75) (Fig.4A-Q''). DRGs of *Smn*$^{2B/-}$ mice showed a significant decrease in neuron soma size in relation to that observed in DRGs of WT littermates (Fig. 4A and B). Although we did not note any significant changes in the number of neurons expressing CGRP or IB4 in the DRGs of *Smn*$^{2B/-}$ animals (Fig. 4C and F), the size of these cell subpopulations was notably reduced (Fig. 4D,E and G,H). Conversely, PV immunoreactive neurons in *Smn*$^{2B/-}$ DRGs did not display any change in size (Fig. 4J,K) but their number significantly decreased (~45% reduction) in relation to that in WT DRGs (Fig. 4I). These data indicate a marked loss of proprioceptive neurons and atrophy of nociceptive subpopulations in the DRG linked to SMA.

We next examined whether alterations in *Smn*$^{2B/-}$ DRG neurons were accompanied by sensory axon defects. L4 DRs, obtained from WT and *Smn*$^{2B/-}$ mice at different time points, were embedded in plastic resin and transversely sectioned. During the early stages of disease (P5 and P10) no phenotypic changes were seen in the sensory axons of *Smn*$^{2B/-}$. However, from P20 onwards, we noted a significant reduction in the DR area in SMA animals (Fig. 5A-C). The number of axons in the DRs was then counted at the end-stage of disease (P25-30). Although moderate axonal loss was found in *Smn*$^{2B/-}$ DRs, this change did not reach a statistically significant level (Fig. 5D). Conversely, compared to WT littermates, *Smn*$^{2B/-}$ mice exhibited a significant decline in the diameter of sensory axons (Fig. 5E-H). The absence of noticeable sensory axon loss in *Smn*$^{2B/-}$ animals could be due to the fact that PV positive proprioceptive neurons, which we found in smaller numbers in SMA, represent only a small proportion (~13%) of the total number of L4 DRG neurons (76). On the other hand, the reduction in size of the sensory

axons observed in SMA mice could result from the cell atrophy observed in other subpopulations of DRG neurons (e.g. CGRP- and IB4-positive neurons).

Reactive gliosis in the spinal cord and MN deafferentation in *Smn$^{2B/-}$* mice

Astroglial and microglial reactions in the ventral horn of spinal cord are changes linked to SMA in humans (38, 77-80) and severe murine models, including SMNΔ7 (49, 50, 60, 80, 81). To study whether glial activation also occurs in the spinal cord of *Smn$^{2B/-}$* mice, we analyzed astroglia and microglia after immunolabeling for GFAP and IBA-1, respectively. Diseased animals showed a progressive astrocytic reaction and prominent microgliosis around MNs. In relation to the ventral horns of WT animals, those of *Smn$^{2B/-}$* mice at P20 showed an increase in GFAP positive profiles which peaked at P25-30; spinal cords of *Smn$^{2B/-}$* animals also exhibited a significantly higher density of IBA1 positive microglia at P20, with only a slight reduction at P25-30 (supplementary Fig. 2A-H).

SMA progression is accompanied by functional and structural alterations in the sensory-motor connectivity, resulting in MN hyperexcitability (27, 49, 82-85). We therefore sought to analyze any changes in afferent synapses on the MNs of the *Smn$^{2B/-}$* mice. To do this, the density of synaptic boutons on the MN somata was quantified in the lumbar spinal cord of WT and diseased animals at different time points. Glutamatergic excitatory and GABAergic inhibitory synapses were identified using antibodies against VGluT1 and VGAT. We found a gradual reduction in the density of both types of synapses as disease progressed. Compared to age-matched WT animals, the number of VGluT1 synapses on the MNs of *Smn$^{2B/-}$* mice was significantly reduced at P20 and, more prominently, at P25-30 (supplementary Fig. 2I-O). The density of VGAT-positive synapses on *Smn$^{2B/-}$* MNs was seen moderately, although significantly

increased at P10. After this age, the VGAT-afferent density on *Smn*$^{2B/-}$ MNs progressively declined, and therefore at P25-30 it was markedly lower than on WT MNs (supplementary Fig 2P and Q-V). The dramatic loss of VGAT-immunoreactive boutons at the end-stages in *Smn*$^{2B/-}$ mice contrasts with previous findings in the SMNΔ7 model, in which no reduction in the number of inhibitory inputs on MNs has been found at the late-symptomatic stages (49, 82).

The potential changes in cholinergic inputs (C-bouton synapses) to MNs in SMA have been less explored (86). C-boutons were immunolabeled using an anti-VAChT antibody. WT mice were found to display a progressive postnatal increase in the number of C-boutons on MNs (Fig. 6A). Whereas MNs of both *Smn*$^{2B/-}$ and WT mice exhibited similar densities of C-boutons from P5 to P20, a dramatic loss of this type of synapse was observed in *Smn*$^{2B/-}$ MNs at P25-30 (Fig. 6A); indeed, at this age, MNs of diseased animals appeared to be almost devoid of cholinergic inputs (Fig. 6B-I). This C-bouton depletion in *Smn*$^{2B/-}$ MNs was not, however, accompanied by any change in their synaptic size (C-bouton area at P25-30 expressed in μm^2: WT = 3.70±0.20, *Smn*$^{2B/-}$ = 3.72±0.14; $p>0.05$, Student's *t*-test, n = 110-170 boutons, 3-4 animals per condition).

We next analyzed the expression of NRG1 and Sig1R, two proteins associated with C-boutons (27, 39, 87, 88), in WT and *Smn*$^{2B/-}$ MNs. We had previously reported that NRG1 expression in spinal cord MNs dramatically decreased during the end-stages of disease in the SOD1^{G93A} mouse model of ALS, but not in SMNΔ7 mice (27). On the other hand, reduced levels of Sig1R in lumbar MNs had been found in SOD1^{G93A} mice, even during early pre-symptomatic stages (89). We used specific antibodies against either NRG1 or Sig1R in combination with VAChT immunostaining to detect C-boutons. The percentage of C-boutons showing positive NRG1 was similar for both WT and *Smn*$^{2B/-}$ MNs at P10 and P20, but was found to significantly fall in *Smn*$^{2B/-}$ MNs at

P25-30 (Fig. 6J and L,M). On the other hand, the expression of Sig1R in C-boutons declined in *Smn*$^{2B/-}$ MNs at P20, and this reduction was maintained at P25-30 (Fig. 6K and O,P). It should be noted that in both WT and *Smn*$^{2B/-}$ P10 mice, Sig1R immunoreactivity was extensively detected in the cytoplasm of MN somata, probably reflecting a high density of ER membranes (Fig. 6Q); even so, only a low percentage of C-boutons contained Sig1R at this age (WT: ~8%, *Smn*$^{2B/-}$: ~9%; $p>0.05$, Student's *t*-test, n = 110-170 synapses; 3-4 mice per condition). At P20, however, the vast majority of WT MNs failed to show any signs of broadly cytoplasmic Sig1R immunostaining; conversely, Sig1R positive profiles were seen postsynaptically associated with VAChT-positive C-boutons. These observations are consistent with previous reports showing that C-bouton-associated Sig1R expression only arises after the second week of postnatal development (88, 90). Nevertheless, the reduction in cytoplasmic Sig1R normally observed at P20 did not occur in most of the MNs of *Smn*$^{2B/-}$ mice (Fig. 6R), apparently pointing to a defective Sig1R maturation process in SMA. A comparable developmental pattern of Sig1R was observed in MNs of SMNΔ7 mice (not shown). Overall, these results demonstrate that, although some cholinergic terminals are still present at later stages of SMA, they do display defects in their postsynaptic molecular organization, such as the reduction in NRG1 and Sig1R expression.

Changes in the NMJs of *Smn*$^{2B/-}$ mice

As previously reported, the NMJs of SMA mice exhibit signs of denervation, NF accumulation and morphological alterations that suggest a delayed synaptic maturation (50, 58, 60, 91-94). In severe mouse models of SMA, these alterations appear to be more prominent in certain muscles in the head and trunk than in those distally located in limbs, which frequently remain fully innervated until later stages of disease (50, 82, 94). To examine whether the NMJs of proximal and distal muscles of *Smn*$^{2B/-}$ mice also

display differential vulnerability, the proportions of NMJ denervation and NF accumulation were examined in IC and TA muscles of WT and *Smn*$^{2B/-}$ mice from P10 to P25-30. To do this, muscles were immunolabeled with antibodies against NF and SV2 to recognize the presynaptic compartment, and then stained with α-Bgtx to identify the postsynaptic site. In relation to WT mice, *Smn*$^{2B/-}$ animals showed a higher percentage of NMJ denervation and NF accumulation in both IC and TA muscles; however, the NMJs of IC muscles appeared to be more severely denervated and exhibited abnormal NF aggregation at an earlier stage than those in TA muscles (supplementary Fig. 3A-D and I-P). In the IC muscles of diseased animals, a significant degree of denervation and NF accumulation was already evident at P10, with this being even more prominent at P20; in contrast, in the TA muscles of *Smn*$^{2B/-}$ mice, the number of NMJs exhibiting NF accumulation was not significant until P20, and then dramatically increased at P25-30 (the age at which significant denervation was also noticed). Interestingly, at P25-30 a reduction in the percentage of denervated NMJs was observed in IC muscles of *Smn*$^{2B/-}$ animals (supplementary Fig. 3A); this suggests that compensatory mechanisms of denervation could exist throughout the course of the disease. In fact, increased levels of axonal sprouting have been observed in the NMJs of different SMA mouse models (50, 60, 91, 95), including those in *Smn*$^{2B/-}$ mice ((96) and our own observations). The architectural analysis of postsynaptic sites also revealed that NMJs of both IC and TA muscles were smaller and less mature in *Smn*$^{2B/-}$ mice than in WT littermates, with a significant increase in the number of NMJs exhibiting a plaque and fold structure and a dramatic reduction in the number of those showing a perforated or pretzel-like (second structure) morphology (supplementary Fig. 3E-H). Overall, these changes also occurred at an earlier stage and were more prominent in IC than in TA muscles. These data, when compared with those reported in SMNΔ7 mice (50, 82, 92-

94) in which hindlimb muscles remained innervated throughout disease progression, suggest that the slower the SMA progression is (as in the *Smn*$^{2B/-}$ mouse model) the greater is the degree of impairment in the NMJs of the distal (e.g. TA) muscles at end-stages.

Chronic treatment with PRE-084 did not improve lifespan or motor abilities in SMA mice

We next wanted to establish whether the clinical SMA phenotype could be prevented or attenuated by the chronic administration of the Sig1R agonist PRE-084. To do this, SMNΔ7 and *Smn*$^{2B/-}$ mice, and their respective WT littermates, were daily treated with either PRE-084 (0.25mg/kg) or saline from P1 onwards. Body weight and survival were measured and a battery of tests was performed to evaluate motor function. As expected, SMNΔ7 and *Smn*$^{2B/-}$ mice treated with saline showed a lower growth-related gain in body weight than saline-injected WT animals. PRE-084 administration did not have any apparent influence on body weight in either of these models or phenotypes (supplementary Fig. 4A and Fig. 7A). The righting reflex and tube test were used to assess muscle strength and motor coordination in SMNΔ7 mice throughout their lifetime, and in *Smn*$^{2B/-}$ animals from P1 to P10. Both saline- and PRE-084-treated SMNΔ7 mice required similar times to right themselves on all 4 paws, demonstrating significant difficulties in righting themselves in comparison with saline- and PRE-084-treated WT mice (supplementary Fig. 4B). Similarly, SMNΔ7 animals, independently of their treatment (either with saline or PRE-084), had shorter latencies to fall and registered worse scores compared to their age-matched WT mice when they were assessed using the tube test (supplementary Fig. 4C). As expected, no differences were observed between *Smn*$^{2B/-}$ animals and their WT littermates when the righting reflex and tube tests were performed from P1 to P10 (data not shown). From P10 onwards, the pen

test and the grip test were applied to assess motor abilities in the *Smn*$^{2B/-}$ model. Compared to WT mice, at P10, the diseased animals presented significantly shorter latencies to fall and lower scores in the pen test; these differences were maintained during the rest of the period studied. Similarly, from P16 on, the *Smn*$^{2B/-}$ animals showed worse performances in the grip test than the WT mice. PRE-084 administration did not produce any significant change in motor abilities of either WT or diseased mice. (Fig. 7B and C).

The Sig1R-agonist treatment was unable to prolong the lifespan of SMNΔ7 or *Smn*$^{2B/-}$ mice: saline- and PRE-084-treated diseased animals showed similar Kaplan-Meier survival curves and mean survival rates (SMNΔ7-saline: 14.67 ± 1.05 days [n= 15] and SMNΔ7-PRE-084: 14.86 ± 1.24 days [n=14], p>0.05, Student's-*t* test; *Smn*$^{2B/-}$-saline: 22.11 ± 0.87 days [n=12] and *Smn*$^{2B/-}$-PRE-084: 21.00 ± 0.79 days [n=12]; p>0.05, Student's-*t* test) (supplementary Fig. 4D and Fig. 7D).

PRE-084 administration did not prevent MN loss or any of the major pathological changes found in the NMJs of *Smn*$^{2B/-}$ mice

We next explored whether PRE-084 treatment was able to prevent MN death in the *Smn*$^{2B/-}$ mouse. We restricted these experiments to this model due to the fact that, as previously mentioned, despite being more prominent, spinal cord MN degeneration in these mice is slower than in SMNΔ7 mice. Lumbar spinal cord MNs were counted in WT and diseased animals at P20. PRE-084 administration did not have any significant effect on MN numbers in *Smn*$^{2B/-}$ mice (Fig. 8A). This treatment did not improve the MN atrophy observed in SMA animals either (MN soma size in μm^2 = *Smn*$^{2B/-}$-saline: 379.6 ± 24.22 [n=25] and *Smn*$^{2B/-}$-PRE-084: 344.7 ± 20.29 [n=22]; p>0.05, Student's-*t*

test). These data contrast with the reported neuroprotective effects of chronic PRE-084 treatment in SOD1^{G93A} mice (41).

As MNJ alterations were more gradual and less severe in the TA muscle, this was used to explore the effect of PRE-084 on neuromuscular histopathology in *Smn*$^{2B/-}$ mice. No significant structural changes in NMJs of PRE-084-treated WT animals were observed in comparison with saline-injected WT mice (not shown). Chronic PRE-084 administration mitigated the aberrant NF accumulation in nerve terminals (Fig. 8B, and J and N), but it did not prevent muscle denervation in diseased animals (Fig. 8C). PRE-084 treatment neither improved the degree of atrophy nor the immaturity of *Smn*$^{2B/-}$ NMJs (Fig. 8D, E, and F-Q). The existence of muscle denervation despite the reduction in NF accumulation in the nerve terminals of PRE-084-treated SMA mice is in agreement with previous findings which suggest that NF aggregation does not correlate with NMJ vulnerability and does not predict subsequent muscle denervation (94).

PRE-084 treatment mitigated reactive gliosis and restored the imbalance of microglial phenotypes associated with SMA

Following chronic PRE-084 treatment, significant reductions in reactive astrogliosis and microgliosis were noted in both SMNΔ7 and *Smn*$^{2B/-}$ mouse models (Fig. 9A-J). When activated in neuroinflammation, microglial cells can develop to one of two opposing maturation states: M1 and M2 phenotypes (97-99). The M1 phenotype has been associated with degeneration and inflammation, while the M2 phenotype has been related to regenerative and anti-inflammatory processes. In neurodegenerative diseases, microglial cells may play either a harmful (M1 phenotype, “classical activation”) or beneficial (M2 phenotype, “alternative activation”) role; this depends on their intrinsic properties, the milieu in which they are activated, and the factors that they are

stimulated by (98, 99). We therefore next examined whether the inhibition of microgliosis by PRE-084 implied the induction of the M2 phenotype. IBA1 immunohistochemistry was combined with Mac-2 or CD206 immunolabeling for M1 and M2 microglia, respectively (100-102). Compared to WT animals, *Smn*$^{2B/-}$ mice were found to exhibit a dramatic increase in harmful M1 (Mac-2-positive) microglia and a significant reduction in regenerative-associated M2 (CD206-positive) cells in the spinal cord. PRE-084 treatment reduced the density of the Mac-2-immunoreactive profiles and enhanced the number of CD206-immunolabeled cells found in *Smn*$^{2B/-}$ spinal cord (Fig. 9K and L, and M-R''). These results indicated that the pharmacological activation of Sig1R prevents the M1/M2 imbalance associated with SMA.

PRE-084 reversed the loss of synaptic afferents to MNs in *Smn*$^{2B/-}$ mice

It had been previously shown that, in pathological conditions, activated microglial cells physically interact with damaged neurons and are able to remove synaptic afferents (reviewed in (103)). As PRE-084 prevents reactive gliosis in the spinal cord of SMA animals, we explored whether this agent was also able to attenuate glial-dependent MN deafferentation. Sections of spinal cord immunolabeled for VAChT, VGluT1 or VGAT were examined in order to quantify the number of positive puncta on the MN somata of P20 WT and *Smn*$^{2B/-}$ animals treated with either saline or the Sig1R agonist. PRE-084 did not significantly change the density of VAChT-immunolabeled synapses compared to MNs of saline-treated *Smn*$^{2B/-}$ animals (Fig. 10A-D'). However, PRE-084-treated *Smn*$^{2B/-}$ mice showed a significant rescue of VGluT1-positive boutons (Fig. 10E-H') and prevented the moderate loss of VGAT synapses (Fig. 10I-L') resulting from disease.

PRE-084 treatment did not modify Sig1R or NRG1 expression in the spinal cord of in *Smn*$^{2B/-}$ mice

Previous studies had reported that Sig1R agonists were able to promote their action by means of Sig1R upregulation via a positive-feedback mechanism (104). We therefore decided to examine whether chronic PRE-084 treatment modulates the expression of Sig1R in *Smn*$^{2B/-}$ mice (Fig. 11A-O). Western-blot analysis, used to determine Sig1R levels in the spinal cord, revealed no significant differences in the amount of this protein between the different experimental groups (Fig. 11A-B). To assess whether PRE-084 affected Sig1R expression in MNs, we performed a double immunofluorescence with antibodies against Sig1R and VAChT (for C-bouton identification) on spinal cord sections from WT and *Smn*$^{2B/-}$ mice. PRE-084 did not modify the reduced numbers of C-boutons associated with Sig1R-positive profiles found in MNs of diseased animals (Fig. 11C-O). NRG1-positive profiles were also quantified in sections that were co-immunostained with anti-NRG1 and anti-VAChT antibodies. MNs of PRE-084- and saline-treated *Smn*$^{2B/-}$ mice exhibited similar numbers of C-boutons expressing NRG1 (Percentage of VAChT-positive boutons associated with NRG1-positive profiles: *Smn*$^{2B/-}$-saline = 88.67±2.39 [n = 40 MNs], *Smn*$^{2B/-}$-PRE-084 = 85.12±3.14 [n=30 MNs]; 4 mice per group; $p>0.05$).

PRE-084 treatment did not modify either the expression levels of SMN or modulate the NMDA receptor in the spinal cord of *Smn*$^{2B/-}$ mice

Western blot analysis was carried out to determine whether the beneficial effects of PRE-084 on reactive gliosis and MN deafferentation seen in SMA were a consequence of an increase in the expression levels of SMN in the spinal cord. Similar low levels of SMN were found in extracts from diseased mice treated with either saline or PRE-084 (Fig. 11 P,Q). A previous *in vitro* study using rat ganglion cells had shown that PRE-084 modulated NMDA receptors (105). It had also been previously reported that the therapeutic effects of PRE-084 on SOD1^{G93A} mice were mediated by the

phosphorylation of the NMDA receptor subunit NR1 at serine-896 and serine-897 (41). Using antibodies against NR1 and p-NR1 (Ser897), we performed western blots of spinal cord extracts from WT and *Smn*$^{2B/-}$ animals treated either with saline or PRE-084. No changes were observed in either total NR1 or p-NR1 protein levels when we compared samples from *Smn*$^{2B/-}$ mice treated with saline and PRE-084 (Fig. 11R-T).

DISCUSSION

In the present study, we used the *Smn*$^{2B/-}$ intermediate mouse model of SMA (43, 44) to provide a detailed characterization of the progression of the histopathological phenotype throughout the disease course, including: MN degeneration, defects in the DRG, changes in spinal cord central synapses, glial reaction and alterations in NMJs. The correlations of these changes with functional motor deficits were also examined. As C-bouton alteration and reactive gliosis were found to be prominent features in *Smn*$^{2B/-}$ mice, we explored the potential therapeutic effects of the Sig1R agonist PRE-084 in this model. The findings were then extrapolated to the SMNΔ7 mouse, a widely used severe model for the disease.

Here we report that *Smn*$^{2B/-}$ mice suffer gradual and prominent MN degeneration in the lumbar spinal cord (>75% of the MNs present in WT animals died), starting during the early-presymptomatic stages of SMA; this contrasts with the moderate (~20%) MN loss found in severe models (*Smn*$^{+/-}$;*SMN2*$^{+/+}$ and SMNΔ7 mice) of the disease (49, 60). We also show that fast MNs are more vulnerable to degeneration in SMA than slow ones. Additionally, we demonstrate structural alterations in motor axons that are already occurring during the early-presymptomatic stages of the disease. Motor axon defects coincide with the onset of MN death and occur in the absence of overt pathological changes in the NMJs of hindlimb muscles. We also report the existence of a dramatic

loss of proprioceptive neurons and atrophy of both peptidergic and non-peptidergic nociceptive neurons in the DRG of *Smn*$^{2B/-}$ mice. Changes in DRG neurons are accompanied by structural defects in sensory axons and the loss of afferent inputs to MNs. We also show, confirming previous findings in the most severe models of SMA, that *Smn*$^{2B/-}$ mice display a prominent reactive gliosis in the spinal cord, which includes a disruption of the M1/M2 microglia phenotype. Chronic PRE-084 treatment attenuates reactive gliosis and restores the altered M1/M2 balance in SMA. This suggests a potential therapeutic effect of the Sig1R agonist by promoting M2 polarization and, in this way, favoring the beneficial anti-inflammatory action of microglia in SMA. This effect correlates with the prevention of the MN deafferentation process which takes place in the course of the disease. However, the beneficial effects of PRE-084 on gliosis and afferent inputs to MNs are not accompanied by either any improvement in lifespan or motor performance; PRE-084 similarly fails to prevent MN loss or to mitigate any of the major pathological changes present in the neuromuscular junctions of SMA mice.

Remodeling and maturation processes occur in the central and peripheral nervous system during the first postnatal weeks (56, 106). Sig1R is enriched in mouse spinal cord MNs, in which the protein is first visualized in the ER at later stages of embryonic development, and then concentrates in C-boutons during the second postnatal week (88, 90). The Sig1R location in C-boutons (88, 107) suggests the involvement of this receptor in the modulation of cholinergic synapses and, as a consequence of this, also in MN excitability and susceptibility to degeneration (20, 21, 108). We found changes in the normal distribution of Sig1R on MN somata and a defect in its association with C-boutons in SMA mice; for instance, whereas at P20 the vast majority of WT MNs exhibited Sig1R in C-boutons with only a minimal cytoplasmic expression of this protein, most of the *Smn*$^{2B/-}$ MNs still displayed extensive cytoplasmic Sig1R

immunoreactivity. These results were, at least in part, comparable to those described in the wobbler mouse, a model for spontaneous MN degeneration (42). A link between *Sig1R* gene mutations and distinct neurodegenerative diseases has been reported (37, 38). Moreover, it has been shown that Sig1R alterations may lead to MN dysfunction and degeneration (39, 109). Reduced levels and an abnormal distribution of Sig1R protein in the spinal cord of patients and mouse models for ALS have also been noticed (41, 110). In our work, we did not detect any altered levels of Sig1R protein in lumbar spinal cord extracts from $Smn^{2B/-}$ mice; however, by immunocytochemistry, we observed a reduced expression of Sig1R at C-boutons in this SMA model at P20, coinciding with the full symptomatic stage. This reduction in the synaptic levels of Sig1R persisted until the terminal stages of the disease. Even so, we did not find any changes in the pattern of Sig1R expression in the pre-symptomatic stages (e.g. at P10). These findings cannot be generically applied to MN diseases because in ALS mice reduced Sig1R levels have been found both in the whole spinal cord and in C-boutons during the early pre-symptomatic stages (41). Although we cannot rule out a role for Sig1R in SMA pathogenesis, the fact that the defects in the motoneuronal expression of this protein did not occur until advanced stages would suggest a late involvement of Sig1R in the neuromuscular dysfunction linked to this disease. This would explain why in $Smn^{2B/-}$ mice, MN loss (~16% of WT) had already been detected at P5, an age at which no significant differences in C-bouton density were found between WT and diseased animals. MN death continued as disease progressed, so at P10 a significant decrease (> 30% of WT) in the number of apparently healthy MNs was seen in SMA mice, but no apparent changes were noted in either the density of C-boutons or the number of those displaying Sig1R-positive immunolabeling. Moreover, the significant reduction in Sig1R expression in C-boutons on $Smn^{2B/-}$ MNs observed at P20 (when ~

65% MNs had already been lost) was not accompanied by changes in C-bouton density on the remaining MNs: whereas in *Smn*$^{2B/-}$ MNs, the reduction in Sig1R expression at C-boutons had already been detected by P20, the loss of VAChT-labeled C-bouton terminals was not seen until P25-30. This indicates a dissociation in the loss of pre- (VAChT) and post-synaptic molecules (Sig1R) at C-boutons. The reduction in Sig1R expression found in C-boutons of *Smn*$^{2B/-}$ MNs is therefore an event that clearly precedes the loss of this type of synapse during the end-stages of the disease, when a large number of MNs had already died.

Given its close proximity to Kv2.1 and to SK channels in C-boutons, Sig1R appears to play a role in the modulation of postsynaptic excitability and, subsequently, MN vulnerability. In fact, in a number of different experimental models, it has been reported that Sig1R can regulate the activity of Kv and SK channels (111, 112) and that Kv2.1 and/or SK channel activation inhibits MN excitability (20, 21, 25, 113). Conversely, increased excitability was found in MNs exhibiting a reduction in Sig1R expression (107). On the other hand, Sig1R has also been involved in the regulation of Ca^{2+} homeostasis by modulating Ca^{2+} entry through plasma membrane (i.e. via voltage-dependent Ca^{2+} channels), and Ca^{2+} flow from ER and to mitochondria (i.e. via inositol triphosphate type 3 [IP3] receptor) (28). Sig1R also appears to modulate NMDA receptor activity (105) and, subsequently, Ca^{2+} influx in neurons. In the present study, the activation of Sig1R by its agonist PRE-084 did not prevent MN degeneration or motor deterioration in *Smn*$^{2B/-}$ mice. These results contrast with the neuroprotective action and improvement in motor performance conferred by PRE-084 in the SOD1^{G93A} (41) and wobbler (42) mouse models of MN disease. Taking into account the fact that these studies used similar dosages, regimens and modes of PRE-084 administration to the ones we used in the present work, it is possible that differences in the rates of

disease progression and in the pathogenic mechanisms could account for the disparities in the results. In fact, both disease models ($SOD1^{G93A}$ and wobbler mice), have a slower clinical outcome with a longer lifespan, and exhibited neuropathological alterations that start later and evolve more gradually than those in $Smn^{2B/-}$ mice ((46, 51, 114, 115), and our own observations). On the other hand, it has also been reported that PRE-084 is able to protect MNs against excitotoxic insults (40) and to prevent MN degeneration in $SOD1^{G93A}$ ALS mice (41) through the modulation of NMDA receptors via the protein kinase C (PKC) pathway. In the latter work, the authors reported a significant increase in the phosphorylation of NMDA-NR1 subunits in spinal cord extracts and also in MNs of mice treated with PRE-084 (41). These findings suggest that the neuroprotective action of PRE-084 could be due to a subsequent reduction in the Ca^{2+} permeability of NMDA receptors and, consequently, to a decrease in the influx of Ca^{2+} into MNs. We did not, however, detect any significant change in NR1-subunit phosphorylation, either by western blotting or by immunohistochemistry, in spinal cord samples from PRE-084-treated $Smn^{2B/-}$ mice. Although we cannot conclude that the absence of a modulatory action on NMDA receptors is responsible for the lack of neuroprotection found after PRE-084 administration in our system, it must be taken into account that the regulation of intracellular Ca^{2+} homeostasis throughout NMDA-receptor modulation is considered a major mechanism through which Sig1R agonists promote neuroprotection (116, 117).

Neuroinflammation, which involves the reactive activation of both microglia and astroglia, is a common process in a number of different neurodegenerative diseases, including ALS (118, 119). Reactive gliosis has also been described in SMA, in both humans (78, 79) and severe mouse models of the disease (49, 82, 120). However, the role of neuroinflammation in SMA pathogenesis has still to be properly elucidated. In fact, the glial reaction associated with neurodegenerative disorders may have either

deleterious (cytotoxic) or beneficial (neuroprotective) effects on MNs ((80, 99, 101) as reviews). Microglia are heterogeneous cells that exhibit different functional states which can be categorized in two opposing phenotypes: M1 (proinflammatory) and M2 (immunosuppressive and neuroprotective). M1 microglia can turn into M2 microglia, and vice versa, depending on the context in which they are activated. This dynamic transformation of M1/M2 phenotypes appears to play a critical role in neurodegeneration. In pathological conditions, neuronal death has therefore been related to a broken balance between the two microglial (M1/M2) subpopulations as a consequence of the sustained activation of M1 cells (99, 101). Similarly, it has recently been reported that neuroinflammation can induce two different subtypes of reactive astrocytes: A1 and A2 (in analogy to the references used for M1 and M2 microglia), (121); whereas A2 astrocytes might be neuroprotective, A1 astrocytes appear to be detrimental and to develop neurotoxic functions following their activation by reactive microglia (121). Here, we show that marked microglia and astroglia activation also occurs in the spinal cord of *Smn*$^{2B/-}$ mice, in which phenotypic and pathological changes linked to SMA take place later and more gradually than in severe mouse models of the disease (48). We also report that microgliosis in SMA is accompanied by a significant increase in M1 microglia at the expense of a reduction in M2 microglia. Moreover, and in agreement with what has been observed in severe SMA mouse models (i.e. SMNΔ7 mice, (49)), reactive gliosis in the spinal cord of *Smn*$^{2B/-}$ animals starts several days after MN degeneration and coincides with the overt loss of glutamatergic excitatory synapses. On the other hand, the reduction in the density of inhibitory GABAergic and cholinergic synapses on *Smn*$^{2B/-}$ MNs is only significant at the end-stages of the disease, some days after the onset of marked and sustained gliosis around degenerating neurons. Overall, these results extend our previous findings regarding severe mouse models of

SMA (49, 60) and support the assumption that microglial cells do not play an active role as inductors of MN degeneration in this disease. Accordingly, we have not observed any significant microgliosis in the spinal cord of *Smn*$^{-/-}$;*SMN2*$^{+/+}$ mice (a SMA model which is more severe than SMNΔ7) at the end-stages of the disease, coinciding with the maximal loss of MNs (60). It is therefore more likely that microgliosis is a secondary, reactive, process resulting from MN dysfunction. In this regard, we found that motor axons of *Smn*$^{2B/-}$ mice undergo overt histopathological changes at as early as P5; this is a time point at which MN loss, although present, is not yet significant and mice do not exhibit any apparent motor disabilities. Alterations in motor axons of P5 *Smn*$^{2B/-}$ mice include: swelling, hypomyelination and Wallerian-like degeneration. These changes may reflect a primary distal alteration ("dying-back") or, alternatively, a secondary response to an earlier MN dysfunction. Whatever the case, altered MNs can create a pathological environment in the spinal cord which is critical for the activation of glial cells and promoting their physical interaction with damaged MNs (103). It is known that, under pathological conditions, microglia play a role not only in removing damaged neurons but also in detaching and engulfing altered afferent synapses, in a process called "synaptic stripping" (122). A similar task has also been described for astrocytes in actively eliminating dysfunctional synapses (123). It has been proposed that synaptic stripping would lead to the disconnection and removal of defective afferent inputs to MNs; this would form part of an attempt to protect them and to leave space to be subsequently occupied by healthy synaptic inputs (124). The time course of glial changes in SMA reported here would favor this role of removing synaptic inputs to MNs. It is well known that the progression of disease in SMA mouse models is associated with functional and structural changes in afferent synapses to MNs (27, 49, 82-85) and that this leads to their progressive deafferentation. We, and others, have

previously reported that, in severe SMA mouse models (e.g. in SMNΔ7 mice), the loss of afferent synapses (and particularly glutamatergic inputs) starts at prenatal ages and precedes MN death (49, 84). Interestingly, we found here that MN deafferentation in *Smn*$^{2B/-}$ mice occurs during the end-stages of the disease and correlates with degenerative changes in DRGs and sensory nerves in the DRs. We therefore observed a significant loss of proprioceptive neurons expressing PV and the atrophy of nociceptive CGRP and IB4 positive neuronal subpopulations in the DRGs of *Smn*$^{2B/-}$ mice at P20. This corresponded with the point when their MNs exhibited a marked reduction in glutamatergic inputs but still retained their GABAergic and cholinergic afferents, which were not significantly reduced in number until P25-30. Importantly, despite the fact that MN death had already started by P5, no apparent structural signs of glutamatergic synapse loss were detected before P20. Although it has been reported that deafferentation does not contribute to MN death in SMA (113), the role of central synapses in the pathogenesis of this disease still remains a subject of discussion (50, 58, 113, 125, 126). In this regard, it has been shown that abnormal MN development due to SMN deficiency results in both MN dysfunction and afferent input defects which can be corrected by expressing SMN in MNs (127). Since MN deafferentation in *Smn*$^{2B/-}$ mice occurs during the end-stages of the disease, in agreement with Fletcher et al.(113), we must conclude that the loss of synaptic afferents is not necessarily linked to MN death. Nevertheless, we cannot exclude the existence of an altered function in remaining central synapses on SMA MNs. In fact, it has been shown that a dysregulation of different MN synaptogenesis genes, which are required for the correct functioning of sensory-motor circuitry, precedes MN pathology (128). It is reasonable to consider that such changes in afferent input activity could have a negative impact on the integrity and function of MNs, thereby contributing to their progressive degeneration and favoring

glial reaction in SMA. It has therefore been reported that, following axotomy, alterations in presynaptic activity would tend to precede MN deafferentation by microglia, a process which appears to play a critical role in MN survival after nerve injury (129).

In the central nervous system, Sig1R is not only expressed in neurons, but also in microglial cells (130) and astrocytes (131). Sig1R stimulation *in vitro* has been found to modulate multiple aspects of microglial activity (including the morphological, migratory and inflammatory responses) (36, 132, 133) and also the inflammatory reaction to several known macrophage activators in the peripheral immune system (134). Sig1R agonists have also been reported to attenuate astrogliosis in a rodent model for stroke injury (135), and to regulate astrocytic activity (136) and the expression of neurotrophic factors following MN injury (34). Here, we show that PRE-084 was able to prevent reactive gliosis in both of the mouse models for SMA (SMNΔ7 and $Smn^{2B/-}$ mice) used in the study. We also found that PRE-084 restored the microglial phenotype (M1/M2) balance altered by the disease. This result is in agreement with the previously reported action of PRE-084 counteracting the M1/M2 imbalance in the wobbler mouse (42). However, contrasting with this finding, the beneficial effect of PRE-084 on neuroinflammation in our model was not accompanied by the prevention of MN degeneration. Nevertheless, we noticed that the Sig1R agonist was able to mitigate the loss of the synaptic inputs that occur in MNs during SMA progression. Overall, these data suggest that the activation of glial Sig1Rs can inhibit the synaptic stripping process resulting from reactive gliosis and show that the prevention of MN deafferentation is not sufficient to inhibit neurodegeneration in SMA. It has been reported that deficient levels of SMN result in intrinsic changes in the functional properties of MNs, which show higher excitability than under normal conditions (85, 137). Moreover, the

restoration of SMN in MNs appears to be necessary for the rescue of electrophysiological deficits in SMA (138). Our results therefore show that the prevention of gliosis and MN deafferentation, resulting from activation of Sig1Rs in the absence of SMN expression in MNs, is not sufficient to promote MN survival or improve motor abilities in SMA. However, pharmacological targeting of glial activation and central synaptic loss should not be neglected as a complementary therapy in conjunction with SMN restoration in SMA, particularly in the less severe forms of disease.

Acknowledgements

We would like to thank Rashmi Kothary for kindly supplying *Smn*$^{2B/2B}$ mice, Justin G. Boyer for advice and suggestions concerning the handling of *Smn*$^{2B/2B}$ animals, Renzo Mancuso for help and suggestions in relation to PRE-084 treatments, Rucsanda Pinteac and Nerea Enara Rodríguez for collaborating in some PRE-084 experiments, Sara Hernández and Sara Salvany for constant support and stimulating discussions, Marta Hereu and Sílvia Gras for technical assistance, Anaïs Panosa for technical support with confocal microscopy, and the *SCT* animal facility of the University of Lleida for mouse care and housing.

FIGURE LEGENDS

Figure 1. MN degeneration in *Smn*$^{2B/-}$ mice. **A, B)** Time-course of MN loss **(A)** and MN atrophy **(B)** in the lumbar spinal cord of *Smn*$^{2B/-}$ mice during disease progression; MN counts and soma area measurements were performed in serial paraffin sections obtained through the entire lumbar segment of spinal cord. MN death **(A)** in *Smn*$^{2B/-}$ animals is already observed at P5, but does not become significant until P10; a dramatic reduction (~75% of WT) in the number of MNs is seen at P20 in *Smn*$^{2B/-}$ animals, with negligible additional MN death from P20 to P25-30. MN death in *Smn*$^{2B/-}$ mice is accompanied by marked atrophy (expressed as a reduction in the soma area) in surviving MNs, which is already significant at P5. **C-G)** Representative images of H&E stained MNs present in the ventral horn of lumbar spinal cord of mice used for cell counting. Note in **(E)** the almost complete disappearance of MNs in the spinal cord of a *Smn*$^{2B/-}$ mouse at the end-stage of disease (P28); contrasting with healthy MNs in WT mice (**C** and **D**), some remaining MNs in *Smn*$^{2B/-}$ animals displayed prominent atrophy and loss of basophilia (arrows in **E** and **F**). Degenerating *Smn*$^{2B/-}$ MNs were frequently surrounded by nuclear profiles presumably corresponding to recruited microglia contacting cell bodies. **H)** Percentage of spinal MNs displaying MMP-9-positive immunoreactivity in WT and *Smn*$^{2B/-}$ mice at different postnatal ages; a significant reduction in the number of MNs expressing MMP-9 (as a marker of the fast MN subtype) can already be observed in SMA animals at P5; the decrease in the percentage of MNs expressing MMP-9 is even more marked in advanced stages of disease. **I-N')** Representative images of lumbar spinal cord sections processed for immunocytochemistry to detect MMP-9 expression (green) in *Smn*$^{2B/-}$ and WT MNs at different postnatal ages; sections were counterstained with fluorescent Nissl staining (red). Note the reduction in MMP-9 levels observed in MNs of *Smn*$^{2B/-}$ animals at all ages, but particularly at P20. The data in the graph are

expressed as mean ± SEM, *p<0.05, **p<0.01 and ***p<0.001 *vs.* WT (two-way ANOVA, Bonferroni's post-hoc test); n = 4-8 mice per age and condition in **(A)** and **(B)**; n = 100-240 MNs of 3-4 animals per age and condition in **(C)**. Scale bars: **E** = 100 μm, (valid for **C**), **F** = 25 μm (valid for **D**), **G** = 10 μm, **J'** = 100 μm (valid for **I-J**), **L'** = 30 μm (valid for **K-L**), **N'** = 20 μm (valid for **M-N**).

Figure 2. Changes in motor axons of *Smn*$^{2B/-}$ mice. **A)** Diameter (in μm) of myelinated axons (including myelin sheath) in L4 VRs of WT and *Smn*$^{2B/-}$ mice at different postnatal ages. **B)** Relative frequency of myelinated axon diameter in L4 VRs of WT and *Smn*$^{2B/-}$ mice at P25-30; in WT VRs there is a clear bimodal profile indicative of axons originating from α-MNs (large axons) and γ-MNs (small axons); note in *Smn*$^{2B/-}$ VRs a selective reduction in the percentage of large axons at the expense of the increased number of small axons. **C)** Number of degenerating motor axons in L4 VRs of WT and *Smn*$^{2B/-}$ mice at different postnatal ages. **D-K)** Representative images taken from semithin cross sections of L4 VRs from WT and *Smn*$^{2B/-}$ mice at different time points. Sections were stained with methylene blue for myelin and axon degeneration analysis. Arrows in (**G**), (**I**) and (**K**) indicate degenerating motor axons. **L)** Percentage of motor axons exhibiting myelin balls in L4 VRs of P5 WT and *Smn*$^{2B/-}$ mice. **M)** Representative images of methylene blue-stained semithin cross sections of VRs from P5 *Smn*$^{2B/-}$ mice used for the counts shown in (**L**); arrows indicate myelin balls inside some motor axons (seen at higher magnification in the inset). The data in the graph are expressed as mean ± SEM; *p<0.05, **p<0.01 and ***p<0.001 *vs.* WT (two-way ANOVA, Bonferroni's post-hoc test in **[A]** and **[C],** and Student's *t*-test in **[L]**; n = 3-5 L4 VRs from different mice per age and condition). Scale bars = 20 μm in **K** (valid for **D-J**) and in **M**; 50 μm in **M** inset.

Figure 3. Ultrastructural analysis of motor axon alterations in *Smn*$^{2B/-}$ mice. **A-F)** Representative electron micrographs of L4 VRs of WT **(A** and **B**) and *Smn*$^{2B/-}$ **(C-F)** animals at P5. **A)** The red arrow indicates a normal Schwann cell enwrapping a healthy motor axon in a WT animal. **B)** The yellow arrow shows one of the very few degenerating axons seen in WT VRs, indicative of a physiological remodeling process during the early postnatal period. **C)** The blue arrow indicates a focal disorganization of myelin lamellae, which results in a multilamellar myelin ball compressing an axon. **D)** The asterisk indicates a swollen axon enwrapped by a thin myelin sheath; another degenerating axon is indicated by the blue arrow. **E)** The asterisk indicates a motor axon enwrapped by a non-myelinating Schwann cell. **F)** A motor axon in an advanced stage of degeneration is indicated by the blue arrow. **G)** Diameter (in μm) of motor axons in L4 VRs from P5 WT and *Smn*$^{2B/-}$ mice, showing a significant increase in the axon size of diseased animals; the measurements were performed by delineating the axon periphery under the myelin sheath. **H, I)** Quantification of myelin thickness by *g*-ratio analysis **(H)** and scatter plot **(I)** depicting *g*-ratios in relation to axon diameter in VRs from P5 WT and *Smn*$^{2B/-}$ animals; note that *Smn*$^{2B/-}$ animals have motor axons with increased *g*-ratios (indicative of thinner myelin sheaths, **H)**, and that these axons correspond to those with greater diameters **(I)**. All the measurements were performed on electron micrographs taken from ultrathin cross sections of L4 VRs at comparable levels. The data in the graphs are expressed as mean ± SEM, ***$p<0.001$ (Student's *t*-test) *vs.* WT; n = 3 L4 VRs from different animals per condition. Scale bar in **E** = 1 μm (valid for **A-D**), and in **F** = 0.5 μm.

Figure 4. Changes in DRG sensory neurons of *Smn*$^{2B/-}$ mice. **A, B)** Neuron size **(A)** (expressed as the soma area in μm^2) and relative frequency distribution of sensory neuron size **(B)** in L4 DRG of WT and *Smn*$^{2B/-}$ mice at P20. **C-K)** Percentage **(C, F** and

I) and soma area **(D, G** and **J)** of sensory neurons expressing CGRP **(C** and **D)**, IB4 **(F** and **G)** and PV **(I** and **J)** in the L4 DRG of WT and *Smn*$^{2B/-}$ mice at P20. **E, H, K)** Relative size-frequency (expressed as soma area in μm^2) histogram of DRG neurons showing CGRP **(E)**, IB4 **(H)** and PV **(K)** positive staining. **L-K'')** Representative micrographs taken from DRG cryostat sections processed for CGRP, IB4 and PV staining (green), as indicated. Sections were also counterstained with fluorescent Nissl staining (red). The data in the graphs are expressed as mean ± SEM; **p*<0.05 and ****p*<0.001 (Student's *t*-test) vs. WT; n = 410-620 neurons counted on 21-26 DRG sections (4 mice per condition). Scale bar in **M''**, **O''** and **K''** = 50 μm (valid for **L-M'**, **N-O'** and **P-K'**, respectively).

Figure 5. Changes in sensory axons in *Smn*$^{2B/-}$ mice. The analysis was performed on L4 DRs. **A**) Area of DRs (in μm^2) from WT and *Smn*$^{2B/-}$ mice at different postnatal ages; n = 3-5 DRs from different mice and conditions. **B, C)** Representative images taken from methylene blue-stained semithin cross sections of DRs from P30 WT **(B)** and *Smn*$^{2B/-}$ **(C)** mice used for the counts shown in **(A)**. **D-F)** Number **(D)** and diameter **(E)** of axons, and relative frequency distribution **(F)** of axon size in DRs from P25-30 WT and *Smn*$^{2B/-}$ mice; n = 250-300 axons of DRs from 3-4 different animals per condition. **G, H)** Representative images showing the appearance of sensory axons analyzed in (**D-F).** All data are expressed as mean ± SEM; **p*<0.05, ***p*<0.01 and ****p*<0.001 *vs.* WT (two-way ANOVA, Bonferroni's post-hoc test **[A]** and Student's *t*-test [**D-F**]); Scale bar in **C** = 50 μm (valid for **B**) and in **H** = 20 μm (valid for **G**).

Figure 6. Changes in C-boutons on lumbar spinal cord MNs of *Smn*$^{2B/-}$ mice. **A)** Density of C-boutons (VAChT-positive puncta) on MNs of WT and *Smn*$^{2B/-}$ mice at different postnatal ages; C-bouton density was calculated after normalization of the synapse number to 100 μm of MN soma perimeter. **B-I)** Representative confocal

micrographs of VAChT-immunoreactive synaptic boutons (green) in the spinal cord ventral horn of WT **(B-H)** and *Smn*$^{2B/-}$ **(C-I)** mice at different ages. Fluorescent Nissl staining (blue) was used for MN identification. **J,K)** Percentage of VAChT-positive boutons associated with NRG1- **(J)** and Sig1R- **(K)** positive profiles in spinal MNs of WT and *Smn*$^{2B/-}$ animals at different postnatal days. **L-P)** Representative confocal micrographs of spinal cord sections processed for double-immunostaining to visualize VAChT (green) and either NRG1 **(L,M)** or Sig1R **(O,P)** (red) in MNs of WT **(L,O)** and *Smn*$^{2B/-}$ **(M,P)** at P20 and P30; fluorescent Nissl staining was used for MN identification (blue); **Q,R)** Confocal images showing the pattern of Sig1R immunoreactivity in MNs of *Smn*$^{2B/-}$ mice at P10 **(Q)** and P20 **(R)**: a broad cytoplasmic Sig1R expression is present in the vast majority of *Smn*$^{2B/-}$ MNs at P10 **(Q)**; this pattern of Sig1R immunostaining, which is downregulated under the control conditions, is still maintained in a high proportion of MNs in P20 *Smn*$^{2B/-}$ animals **(R).** To improve Sig1R visualization settings for red channel were modified in **(Q)** and **(R).** The data in the graphs are expressed as mean ± SEM; n = 30-60 MNs per mice and condition (3-4 animals per age and experimental group); *p<0.05 and ***p<0.001 (two-way ANOVA, Bonferroni's post-hoc test) *vs.* WT. Scale bar: 20 μm in **I** (valid for **B-H**) and **R** (valid for **L-Q**).

Figure 7. Chronic treatment with PRE-084 does not improve lifespan or motor abilities in *Smn*$^{2B/-}$ mice. **A-C)** Body weight curve **(A)**, and pen and **(B)** grip **(C)** tests performed on WT and *Smn*$^{2B/-}$ animals treated with either saline or PRE-084. Values are shown as mean ± SEM, n = 10-12 mice per condition; no significant differences in body weight, or pen and grip test performance were observed between saline- and PRE-084-treated *Smn*$^{2B/-}$ animals (two-way ANOVA, Bonferroni's post-hoc test). **D)** Kaplan-Meier survival curve for the different experimental groups. Saline- and PRE-084-injected

Smn$^{2B/-}$ mice do not show any significant differences in mean survival (22.11 ± 0.87 and 21.00 ± 0.79 days, respectively; $p>0.05$, Student's *t*-test, n = 12 animals per condition). Since no significant differences were observed between saline- and PRE-084 treated WT mice in any of the tests used to assess motor behavior, data from the PRE-084 WT group were excluded to simplify the graphs.

Figure 8. PRE-084 administration does not mitigate MN loss or major pathological changes in NMJs of *Smn*$^{2B/-}$ mice. The data in the graphs, expressed as mean ± SEM, were obtained from the lumbar spinal cord and TA muscles of P20 WT and *Smn*$^{2B/-}$ mice chronically treated with either saline or PRE-084. **A)** Number of apparently healthy MNs in the entire lumbar segment of spinal cord from 5-6 animals per condition. **B-E)** show: percentage of NMJs with NF accumulation in nerve terminals **(B)**, percentage of NMJs exhibiting different degrees of innervation (based on the proportion of α-Bgtx labeled postsynaptic site area covered by SV2-immunostained presynaptic terminals, **C)**, NMJ size (in μm^2, **D)**, and percentage of NMJs showing different degrees of maturity based on the morphology of the postsynaptic site (plaque, folds, perforations or secondary structure [pretzel-like], **E)**; note that the only significant beneficial change induced by PRE-084 in NMJs of *Smn*$^{2B/-}$ animals was the alleviation of NF aggregation in the nerve terminals. Analyses were performed in 50-75 NMJs of TA muscles from 4 animals per condition; ***$p<0.001$ (one-way ANOVA, Bonferroni's post-hoc test). **F-Q)** Representative confocal images illustrating the results shown in **(B-E)**; cryostat sections of TA muscles were immunolabeled with antibodies against NF (blue) and SV2 (red), and stained with α-Bgtx (green) to identify postsynaptic sites. The white arrow in **(J)** indicates NF aggregates in a NMJ of a *Smn*$^{2B/-}$ mouse; yellow arrows in **(K)** and **(O)** indicate denervated NMJs displaying negative

immunostaining for SV2. Dotted lines delineate NMJs. Scale bar in **Q** = 20 μm (valid for **F-M**).

Figure 9. Chronic PRE-084 administration prevents reactive gliosis and restores the microglia phenotype imbalance associated with SMA. **A-D)** Quantification of GFAP-positive astroglia **(A** and **C)** and IBA1-positive microglia **(B** and **D)** around MNs in the ventral horn of lumbar spinal cord from P7-8 SMNΔ7 **(A** and **B)** and P20 *Smn*$^{2B/-}$ **(C** and **D)** mice and their respective WT littermates. **E-J)** Representative confocal micrographs taken from spinal cord sections of WT and *Smn*$^{2B/-}$ used for data analysis in **(C)** and **(D)**; cryostat sections were immunolabeled with antibodies against GFAP and IBA1, (both in green) and counterstained with fluorescent Nissl stain (red); note the significant reduction in both GFAP and IBA1 immunoreactivity around MNs of *Smn*$^{2B/-}$ animals after PRE-084 treatment. **K,L)** Quantification of Mac-2-positive **(K)** and CD206-positive **(L)** immunostaining in the lumbar spinal cord of animals belonging to different experimental groups; note that the significant increase in the number Mac-2-positive (M1) microglia and decrease in CD206-positive (M2) microglia observed in *Smn*$^{2B/-}$ animals is prevented by PRE-084 treatment. **M-R'')** Representative confocal micrographs used for data analysis shown in **(K)** and **(L)**; cryostat sections of lumbar spinal cord from WT and *Smn*$^{2B/-}$ mice, treated with either saline or PRE-084, were processed for immunocytochemistry with antibodies against IBA1 (green) and either Mac-2 or CD206 (red); arrows in **(P')**, **(Q')** and **(R')** indicate CD206-positive cells located in the periphery of the spinal cord white matter, as previously reported (42); note that the number of these cells decreases in sections of *Smn*$^{2B/-}$ mice; this change is restored after PRE-084 treatment. Dotted and dashed lines in pictures delimitate the boundaries of gray matter and white matter (spinal cord section periphery), respectively. The data in the graphs are expressed as mean ± SEM; n = 4 animals per condition in

each genotype; *p<0.05, **p<0.01 and ***p<0.001 (one-way ANOVA, Bonferroni's post-hoc test). Scale bars =200 μm in **G** and **J** (valid for **E** and **F**, and **H-I**, respectively), and in **R''** (valid for **M-R'**).

Figure 10. PRE-084 treatment prevents deafferentation of spinal cord MNs in *Smn*$^{2B/-}$ mice. **A-L')** Number of VAChT **(A)**, VGluT1 **(E)** and VGAT **(I)** puncta apposed to WT and *Smn*$^{2B/-}$ MNs (per 100 μm of soma perimeter) following either saline or PRE-084 injections. The data in the graphs are expressed as mean ± SEM. Counts were performed in 25-40 MNs per mouse (4 animals per condition); *p<0.05 and **p<0.01 (one-way ANOVA, Bonferroni's post-hoc test). Representative confocal images of data included in **(A)**, **(E)** and **(I)** are shown on the right of the graphs; images were taken from sections of lumbar spinal cord processed for immunocytochemistry with antibodies against VAChT **(B-D')**, VGluT1 **(F-H)** and VGAT **(J-L')** (all in green) and counterstained with fluorescent Nissl stain (blue). Scale bar in **L'** = 20 μm (valid for **B-D'**, **F-H'**, and **J-L**).

Figure 11. PRE-084 treatment neither modifies Sig1R and SMN protein levels nor modulates NMDA receptor in the spinal cord of *Smn*$^{2B/-}$ mice. Spinal cords of WT and diseased animals, treated with either saline or PRE-084, were collected at P20 for analysis. **A)** Representative western blots for Sig1R and β-actin (as a loading control). **B)** Quantification by densitometry of Sig1R levels in western blots performed on samples from different conditions. The data are expressed as the percentage of change in relation to the levels found in the WT-saline group. **C)** Percentage of VAChT-positive boutons showing a spatial relationship with Sig1R-positive profiles. **D-O)** Representative confocal images taken from spinal cord sections double immunolabeled with antibodies against VAChT (green) and Sig1R (red) and counterstained with fluorescent Nissl stain for MN identification (blue). **P-T)** PRE-084 treatment does not

modify either SMN or NMDA-receptor levels in the spinal cord of *Smn*$^{2B/-}$ mice. **P)** Representative western blot for SMN and β-actin (as a loading control) in the spinal cord of mice belonging to different groups. **Q)** Densitometry analysis of SMN protein levels in western blots; data are shown as the percentage of change in relation to the ratio of SMN to β-actin of saline-treated WT mice. **R)** Representative western blot for NR1, p-NR1 and β-actin (as loading control) in the spinal cord. **S,T)** Densitometry analysis of NR1 **(S)** and p-NR1 **(T)** protein levels in western blots; the data are shown as the percentage of change in relation to the ratio of either NR1 or p-NR1 to β-actin in the saline-treated WT group. The data in the graph are expressed as mean ± SEM and obtained from 3 mice per condition; $^{**}p<0.01$ and $^{***}p<0.001$ (one-way ANOVA, Bonferroni's post-hoc test). Scale bar in **O** = 10 μm (valid for **D-N**).

Supplementary Figures

Supplementary Figure 1. A-E) Battery of tests used to assess the motor phenotype in *Smn*$^{2B/-}$ mice and their respective age-matched WT littermates, as indicated. **A)** *Smn*$^{2B/-}$ and WT mice show similar body weights until P10, but thereafter *Smn*$^{2B/-}$ animals exhibit smaller sizes and significantly lower weights than their WT littermates, indicative of a reduced growth rate linked to the disease. Righting reflex **(B)** and tube test (latency to fall in seconds **[C])** performed from P1 to P10 (the ideal animal age range for these tests (53)) does not show apparent differences between WT and *Smn*$^{2B/-}$ animals. Pen **(D)** and grip **(E)** tests, performed to assess motor balance and muscular strength, reveal significant differences between WT and *Smn*$^{2B/-}$ mice from P12-P14 onwards. In all the graphs, values are shown as mean ± SEM and two-way ANOVA (Bonferroni's post-hoc test) was used for statistical analysis (n=10-15 mice per experimental group); $^{**}p<0.01$ and $^{***}p<0.001$ *vs.* WT.

Supplementary Figure 2. A-H) Changes in GFAP and IBA1 immunoreactivity in the spinal cord of *Smn*$^{2B/-}$ mice. **A,B)** Quantification of GFAP (for astroglia [**A]**) and IBA1 (for microglia **[B]**) immunoreactivity in the ventral horn of lumbar spinal cord of WT and *Smn*$^{2B/-}$ mice at different postnatal ages; bars in graphs represent the percentage of positive immunoreactivity change in the ventral horn of *Smn*$^{2B/-}$ mice with respect to age-matched WT animals. Image analysis was performed in 15-30 sections per condition (3-4 animals per age and genotype); the data are expressed as mean ± SEM; $^{**}p<0.01$ and $^{***}p<0.001$ (one-way ANOVA, Bonferroni's post-hoc test) *vs.* WT mice. **C-H)** Representative confocal micrographs used for the analysis shown in **(A)** and **(B)**; sections were processed for immunocytochemistry using antibodies against GFAP (**C** and **D**) or IBA1 (**E-H**) (both in green), and counterstained with fluorescent Nissl stain (red); micrographs from P20 and P30 spinal cords are shown. **I-V)** Changes in VGluT1 and VGAT afferent inputs to MNs in *Smn*$^{2B/-}$ mice. **I, P)** Numbers of VGluT1- **(I)** and VGAT- **(P)** positive boutons (puncta) on MNs (per 100 μm soma perimeter) in the lumbar spinal cord of WT and diseased animals at indicated postnatal ages. Bars in graphs represent the percentage of bouton density change in the ventral horn of *Smn*$^{2B/-}$ mice with respect to age-matched WT animals; n = 40-55 MNs per mouse and condition (3-4 animals per age and experimental group). The data are expressed as mean ± SEM; $^{*}p<0.05$, $^{**}p<0.01$ and $^{***}p<0.001$ (one-way ANOVA, Bonferroni's post-hoc test) *vs.* WT mice. **J-V)** Representative confocal micrographs of VGluT1- **(J-O)** and VGAT- **(Q-N)** immunoreactive synaptic boutons (green) in the spinal cord ventral horn of WT **(J-L** and **Q-S)** and *Smn*$^{2B/-}$ **(M-O** and **T-V)** mice; MNs were identified following fluorescent Nissl staining (red). Scale bar: in **D** and **H**= 200 μm (valid for **C** and **E-F**, respectively) and **V** = 20 μm (valid for **J-U**).

Supplementary Figure 3. Progression of NMJ pathology in *Smn*$^{2B/-}$ mice. Pre- and post-synaptic morphology were examined in NMJs of IC and TA muscles at different postnatal ages. **A,B)** Percentage of innervated NMJs in IC **(A)** and TA **(B)** muscles. **C,D)** Number of NMJs showing NF aggregates in IC **(C)** and TA **(D)** muscles. **E,F)** Size (in μm^2) of NMJs in IC **(E)** and TA **(F)** muscles. **G,H)** Percentage of NMJs exhibiting a mature appearance, assessed by the pretzel-like morphology of the postsynaptic site, in IC **(G)** and TA **(H)** muscles; note the significant reduction in the number of mature (pretzel-like) NMJs in both muscles but particularly in IC muscles, in which changes reflecting NMJ immaturity occur earlier and more prominently than in TA muscles. **G-L)** Representative images illustrating the results shown in **(A-H)**; cryostat muscle sections were immunolabeled with antibodies against SV2 and NF (blue), and stained with α-Bgtx (green). **I-K)** show the appearance of healthy NMJs in IC muscles of P10 **(I-J)** and P30 **(K)** WT mice. **L** and **M)** show a denervated NMJ **(L)** and NF accumulation in the nerve terminal of an innervated NMJ **(**arrow in **M)** in IC muscles from P10 *Smn*$^{2B/-}$ mice; an innervated NMJ in the IC muscle of a *Smn*$^{2B/-}$ mouse is depicted in **(N)**; note that although the NMJ has an almost normal appearance, its postsynaptic site is reduced in size. **O-P)** show NMJs in the TA muscle from P20 WT **(O)** and *Smn*$^{2B/-}$ **(P)** mice; note the pretzel-like morphology (indicative of maturity) of the NMJ in **(O)**, and the plaque morphology and dramatic reduction in size of the NMJ in **(P).** The data in the graphs are expressed as mean ± SEM; n = 60-90 NMJs in IC and TA muscles of 3-4 different animals per condition; *p<0.05, **p<0.01, and ***p<0.001 (two-way ANOVA, Bonferroni's post-hoc test). Scale bar: 10 μm in **P** (valid for **I-O**).

Supplementary Figure 4. Chronic treatment with PRE-084 does not improve the motor abilities or lifespan of SMNΔ7 mice. **A-C)** Body weight curve **(A)**, and righting reflex and **(B)** tube test **(C)** performed on WT and SMNΔ7 animals treated with either saline

or PRE-084. Values are shown as mean ± SEM, n = 15-20 mice per condition; no significant differences in body weight, righting reflex or tube test performance were observed between saline- and PRE-084-treated SMNΔ7 animals (two-way ANOVA, Bonferroni's post-hoc test). **D)** Kaplan-Meier survival curve for the different experimental groups. Saline- and PRE-084-injected SMNΔ7 mice does not show any significant differences in mean survival (14.67 ± 1.05 days [n= 15]; SMNΔ7-PRE-084: 14.86 ± 1.24 days [n=14]; $p>0.05$, Student's *t*-test). Since no significant differences were observed between saline- and PRE-084 treated WT mice in any of the tests used for motor behavior examination, data from the PRE-084 WT group were excluded to simplify the graphs.

REFERENCES

1. Sumner CJ. Molecular mechanisms of spinal muscular atrophy. *J Child Neurol* 2007;22:979-89

2. Prior TW, Snyder PJ, Rink BD, et al. Newborn and carrier screening for spinal muscular atrophy. *Am J Med Genet A* 2010;152A:1608-16

3. Sugarman EA, Nagan N, Zhu H, et al. Pan-ethnic carrier screening and prenatal diagnosis for spinal muscular atrophy: clinical laboratory analysis of >72,400 specimens. *Eur J Hum Genet* 2012;20:27-32

4. Lefebvre S, Burglen L, Reboullet S, et al. Identification and characterization of a spinal muscular atrophy-determining gene. *Cell* 1995;80:155-65

5. Coady TH, Lorson CL. SMN in spinal muscular atrophy and snRNP biogenesis. *Wiley Interdisciplinary Reviews-Rna* 2011;2:546-64

6. Lorson CL, Hahnen E, Androphy EJ, et al. A single nucleotide in the SMN gene regulates splicing and is responsible for spinal muscular atrophy. *Proceedings of the National Academy of Sciences of the United States of America* 1999;96:6307-11

7. Coovert DD, Le TT, McAndrew PE, et al. The survival motor neuron protein in spinal muscular atrophy. *Hum Mol Genet* 1997;6:1205-14

8. Lefebvre S, Burlet P, Liu Q, et al. Correlation between severity and SMN protein level in spinal muscular atrophy. *Nature Genetics* 1997;16:265-9

9. Nurputra DK, Lai PS, Harahap NI, et al. Spinal muscular atrophy: from gene discovery to clinical trials. *Ann Hum Genet* 2013;77:435-63

10. Wirth B, Garbes L, Riessland M. How genetic modifiers influence the phenotype of spinal muscular atrophy and suggest future therapeutic approaches. *Curr Opin Genet Dev* 2013;23:330-8

11. Van Alstyne M, Pellizzoni L. Advances in modeling and treating spinal muscular atrophy. *Curr Opin Neurol* 2016;29:549-56

12. Bowerman M, Becker CG, Yanez-Munoz RJ, et al. Therapeutic strategies for spinal muscular atrophy: SMN and beyond. *Dis Model Mech* 2017;10:943-54

13. Singh NK, Singh NN, Androphy EJ, et al. Splicing of a critical exon of human survival motor neuron is regulated by a unique silencer element located in the last intron. *Molecular and Cellular Biology* 2006;26:1333-46

14. Finkel RS, Chiriboga CA, Vajsar J, et al. Treatment of infantile-onset spinal muscular atrophy with nusinersen: a phase 2, open-label, dose-escalation study. *Lancet* 2016;388:3017-26

15. Chiriboga CA, Swoboda KJ, Darras BT, et al. Results from a phase 1 study of nusinersen (ISIS-SMN(Rx)) in children with spinal muscular atrophy. *Neurology* 2016;86:890-7

16. Pechmann A, Langer T, Wider S, et al. Single-center experience with intrathecal administration of Nusinersen in children with spinal muscular atrophy type 1. *Eur J Paediatr Neurol* 2018;22:122-7

17. Finkel RS, Mercuri E, Darras BT, et al. Nusinersen versus Sham Control in Infantile-Onset Spinal Muscular Atrophy. *N Engl J Med* 2017;377:1723-32

18. Tu WY, Simpson JE, Highley JR, et al. Spinal muscular atrophy: Factors that modulate motor neurone vulnerability. *Neurobiol Dis* 2017;102:11-20

19. Roselli F, Caroni P. From intrinsic firing properties to selective neuronal vulnerability in neurodegenerative diseases. *Neuron* 2015;85:901-10

20. Miles GB, Hartley R, Todd AJ, et al. Spinal cholinergic interneurons regulate the excitability of motoneurons during locomotion. *Proc Natl Acad Sci U S A* 2007;104:2448-53

21. Zagoraiou L, Akay T, Martin JF, et al. A cluster of cholinergic premotor interneurons modulates mouse locomotor activity. *Neuron* 2009;64:645-62

22. Conradi S. Ultrastructure and distribution of neuronal and glial elements on the motoneuron surface in the lumbosacral spinal cord of the adult cat. *Acta Physiol Scand Suppl* 1969;332:5-48

23. Hellstrom J, Oliveira AL, Meister B, et al. Large cholinergic nerve terminals on subsets of motoneurons and their relation to muscarinic receptor type 2. *J Comp Neurol* 2003;460:476-86

24. Muennich EA, Fyffe RE. Focal aggregation of voltage-gated, Kv2.1 subunit-containing, potassium channels at synaptic sites in rat spinal motoneurones. *J Physiol* 2004;554:673-85

25. Deardorff AS, Romer SH, Deng Z, et al. Expression of postsynaptic Ca2+-activated K+ (SK) channels at C-bouton synapses in mammalian lumbar -motoneurons. *J Physiol* 2013;591:875-97

26. Mavlyutov TA, Epstein ML, Andersen KA, et al. The Sigma-1 Receptor Is Enriched in Postsynaptic Sites of C-Terminals in Mouse Motoneurons. An Anatomical and Behavioral Study. *Neuroscience* 2010;167:247-55

27. Gallart-Palau X, Tarabal O, Casanovas A, et al. Neuregulin-1 is concentrated in the postsynaptic subsurface cistern of C-bouton inputs to alpha-motoneurons and altered during motoneuron diseases. *FASEB J* 2014;28:3618-32

28. Hayashi T, Su TP. Sigma-1 receptor chaperones at the ER-mitochondrion interface regulate Ca(2+) signaling and cell survival. *Cell* 2007;131:596-610

29. Su TP, Hayashi T, Maurice T, et al. The sigma-1 receptor chaperone as an inter-organelle signaling modulator. *Trends in Pharmacological Sciences* 2010;31:557-66

30. Tsai SY, Pokrass MJ, Klauer NR, et al. Sigma-1 receptor chaperones in neurodegenerative and psychiatric disorders. *Expert Opin Ther Targets* 2014;18:1461-76

31. Kourrich S, Hayashi T, Chuang JY, et al. Dynamic interaction between sigma-1 receptor and Kv1.2 shapes neuronal and behavioral responses to cocaine. *Cell* 2013;152:236-47

32. Monnet FP. Sigma-1 receptor as regulator of neuronal intracellular Ca2+: clinical and therapeutic relevance. *Biol Cell* 2005;97:873-83

33. Maurice T, Su TP. The pharmacology of sigma-1 receptors. *Pharmacol Ther* 2009;124:195-206

34. Penas C, Pascual-Font A, Mancuso R, et al. Sigma receptor agonist 2-(4-morpholinethyl)1 phenylcyclohexanecarboxylate (Pre084) increases GDNF and BiP expression and promotes neuroprotection after root avulsion injury. *J Neurotrauma* 2011;28:831-40

35. Wegleiter K, Hermann M, Posod A, et al. The sigma-1 receptor agonist 4-phenyl-1-(4-phenylbutyl) piperidine (PPBP) protects against newborn excitotoxic brain injury by stabilizing the mitochondrial membrane potential in vitro and inhibiting microglial activation in vivo. *Exp Neurol* 2014;261:501-9

36. Zhao J, Ha Y, Liou GI, et al. Sigma receptor ligand, (+)-pentazocine, suppresses inflammatory responses of retinal microglia. *Invest Ophthalmol Vis Sci* 2014;55:3375-84

37. Luty AA, Kwok JB, Dobson-Stone C, et al. Sigma nonopioid intracellular receptor 1 mutations cause frontotemporal lobar degeneration-motor neuron disease. *Ann Neurol* 2010;68:639-49

38. Al-Saif A, Al-Mohanna F, Bohlega S. A mutation in sigma-1 receptor causes juvenile amyotrophic lateral sclerosis. *Ann Neurol* 2011;70:913-9

39. Mavlyutov TA, Epstein ML, Verbny YI, et al. Lack of sigma-1 receptor exacerbates ALS progression in mice. *Neuroscience* 2013;240:129-34

40. Guzmán-Lenis MS, Navarro X, Casas C. Selective Sigma Receptor Agonist 2-(4-Morpholinethyl)1-Phenylcyclohexanecarboxylate (Pre084) Promotes Neuroprotection and Neurite Elongation through Protein Kinase C (Pkc) Signaling on Motoneurons. *Neuroscience* 2009;162:31-8

41. Mancuso R, Olivan S, Rando A, et al. Sigma-1R agonist improves motor function and motoneuron survival in ALS mice. *Neurotherapeutics* 2012;9:814-26

42. Peviani M, Salvaneschi E, Bontempi L, et al. Neuroprotective effects of the Sigma-1 receptor (S1R) agonist PRE-084, in a mouse model of motor neuron disease not linked to SOD1 mutation. *Neurobiol Dis* 2014;62:218-32

43. Bowerman M, Beauvais A, Anderson CL, et al. Rho-kinase inactivation prolongs survival of an intermediate SMA mouse model. *Hum Mol Genet* 2010;19:1468-78

44. Bowerman M, Anderson CL, Beauvais A, et al. SMN, profilin IIa and plastin 3: a link between the deregulation of actin dynamics and SMA pathogenesis. *Mol Cell Neurosci* 2009;42:66-74

45. DiDonato CJ, Lorson CL, De Repentigny Y, et al. Regulation of murine survival motor neuron (Smn) protein levels by modifying Smn exon 7 splicing. *Hum Mol Genet* 2001;10:2727-36

46. Bowerman M, Murray LM, Beauvais A, et al. A critical smn threshold in mice dictates onset of an intermediate spinal muscular atrophy phenotype associated with a distinct neuromuscular junction pathology. *Neuromuscul Disord* 2012;22:263-76

47. Le TT, Pham LT, Butchbach ME, et al. SMNDelta7, the major product of the centromeric survival motor neuron (SMN2) gene, extends survival in mice with spinal muscular atrophy and associates with full-length SMN. *Hum Mol Genet* 2005;14:845-57

48. Sleigh JN, Gillingwater TH, Talbot K. The contribution of mouse models to understanding the pathogenesis of spinal muscular atrophy. *Dis Model Mech* 2011;4:457-67

49. Tarabal O, Caraballo-Miralles V, Cardona-Rossinyol A, et al. Mechanisms involved in spinal cord central synapse loss in a mouse model of spinal muscular atrophy. *J Neuropathol Exp Neurol* 2014;73:519-35

50. Cerveró C, Montull N, Tarabal O, et al. Chronic Treatment with the AMPK Agonist AICAR Prevents Skeletal Muscle Pathology but Fails to Improve Clinical Outcome in a Mouse Model of Severe Spinal Muscular Atrophy. *Neurotherapeutics* 2016;13:198-216

51. Eshraghi M, McFall E, Gibeault S, et al. Effect of genetic background on the phenotype of the Smn2B/- mouse model of spinal muscular atrophy. *Hum Mol Genet* 2016;25:4494-506

52. Schrank B, Gotz R, Gunnersen JM, et al. Inactivation of the survival motor neuron gene, a candidate gene for human spinal muscular atrophy, leads to massive cell death in early mouse embryos. *Proc Natl Acad Sci U S A* 1997;94:9920-5

53. El-Khodor BF, Edgar N, Chen A, et al. Identification of a battery of tests for drug candidate evaluation in the SMNDelta7 neonate model of spinal muscular atrophy. *Exp Neurol* 2008;212:29-43

54. Willmann R, Dubach J, Chen K, et al. Developing standard procedures for pre-clinical efficacy studies in mouse models of spinal muscular atrophy: report of the expert workshop "Pre-clinical testing for SMA", Zurich, March 29-30th 2010. *Neuromuscul Disord* 2011;21:74-7

55. Brooks SP, Dunnett SB. Tests to assess motor phenotype in mice: a user's guide. *Nat Rev Neurosci* 2009;10:519-29

56. Clarke PGH, Oppenheim RW. Neuron Death in Vertebrate Development - in-Vivo Methods. *Methods in Cell Biology, Vol 46* 1995;46:277-321

57. Calderó J, Ciutat D, Lladó J, et al. Effects of excitatory amino acids on neuromuscular development in the chick embryo. *J Comp Neurol* 1997;387:73-95

58. Gogliotti RG, Quinlan KA, Barlow CB, et al. Motor neuron rescue in spinal muscular atrophy mice demonstrates that sensory-motor defects are a consequence, not a cause, of motor neuron dysfunction. *J Neurosci* 2012;32:3818-29

59. Liu H, Yazdani A, Murray LM, et al. The Smn-independent beneficial effects of trichostatin A on an intermediate mouse model of spinal muscular atrophy. *PLoS One* 2014;9:e101225

60. Dachs E, Hereu M, Piedrafita L, et al. Defective neuromuscular junction organization and postnatal myogenesis in mice with severe spinal muscular atrophy. *J Neuropathol Exp Neurol* 2011;70:444-61

61. Pun S, Santos AF, Saxena S, et al. Selective vulnerability and pruning of phasic motoneuron axons in motoneuron disease alleviated by CNTF. *Nat Neurosci* 2006;9:408-19

62. Nijssen J, Comley LH, Hedlund E. Motor neuron vulnerability and resistance in amyotrophic lateral sclerosis. *Acta Neuropathol* 2017;133:863-85

63. Kaplan A, Spiller KJ, Towne C, et al. Neuronal matrix metalloproteinase-9 is a determinant of selective neurodegeneration. *Neuron* 2014;81:333-48

64. Ito Y, Shibata N, Saito K, et al. New insights into the pathogenesis of spinal muscular atrophy. *Brain Dev* 2011;33:321-31

65. Slater CR. Postnatal maturation of nerve-muscle junctions in hindlimb muscles of the mouse. *Dev Biol* 1982;94:11-22

66. Colman H, Nabekura J, Lichtman JW. Alterations in synaptic strength preceding axon withdrawal. *Science* 1997;275:356-61

67. Saxena S, Caroni P. Mechanisms of axon degeneration: from development to disease. *Prog Neurobiol* 2007;83:174-91

68. Turney SG, Lichtman JW. Reversing the outcome of synapse elimination at developing neuromuscular junctions in vivo: evidence for synaptic competition and its mechanism. *PLoS Biol* 2012;10:e1001352

69. Marshall A, Duchen LW. Sensory system involvement in infantile spinal muscular atrophy. *J Neurol Sci* 1975;26:349-59

70. Murayama S, Bouldin TW, Suzuki K. Immunocytochemical and ultrastructural studies of Werdnig-Hoffmann disease. *Acta Neuropathol* 1991;81:408-17

71. Munsat TL, Davies KE. International SMA consortium meeting. (26-28 June 1992, Bonn, Germany). *Neuromuscul Disord* 1992;2:423-8

72. Jablonka S, Karle K, Sandner B, et al. Distinct and overlapping alterations in motor and sensory neurons in a mouse model of spinal muscular atrophy. *Hum Mol Genet* 2006;15:511-8

73. Antal M, Freund TF, Polgar E. Calcium-binding proteins, parvalbumin- and calbindin-D 28k-immunoreactive neurons in the rat spinal cord and dorsal root ganglia: a light and electron microscopic study. *J Comp Neurol* 1990;295:467-84

74. Fang X, Djouhri L, McMullan S, et al. Intense isolectin-B4 binding in rat dorsal root ganglion neurons distinguishes C-fiber nociceptors with broad action potentials and high Nav1.9 expression. *J Neurosci* 2006;26:7281-92

75. Marmigère F, Ernfors P. Specification and connectivity of neuronal subtypes in the sensory lineage. *Nat Rev Neurosci* 2007;8:114-27

76. Zacharová G, Palecek J. Parvalbumin and TRPV1 receptor expression in dorsal root ganglion neurons after acute peripheral inflammation. *Physiol Res* 2009;58:305-9

77. Chou SM. Glial bundles of nerve roots in Werdnig-Hoffmann disease. *Ann Neurol* 1980;8:79-82

78. Kumagai T, Hashizume Y. Morphological and morphometric studies on the spinal cord lesion in Werdnig-Hoffmann disease. *Brain Dev* 1982;4:87-96

79. Kuru S, Sakai M, Konagaya M, et al. An autopsy case of spinal muscular atrophy type III (Kugelberg-Welander disease). *Neuropathology* 2009;29:63-7

80. Papadimitriou D, Le Verche V, Jacquier A, et al. Inflammation in ALS and SMA: sorting out the good from the evil. *Neurobiol Dis* 2010;37:493-502

81. Rindt H, Feng Z, Mazzasette C, et al. Astrocytes influence the severity of spinal muscular atrophy. *Hum Mol Genet* 2015;24:4094-102

82. Ling KK, Lin MY, Zingg B, et al. Synaptic defects in the spinal and neuromuscular circuitry in a mouse model of spinal muscular atrophy. *PLoS One* 2010;5:e15457

83. Park GH, Maeno-Hikichi Y, Awano T, et al. Reduced survival of motor neuron (SMN) protein in motor neuronal progenitors functions cell autonomously to cause spinal muscular atrophy in model mice expressing the human centromeric (SMN2) gene. *J Neurosci* 2010;30:12005-19

84. Mentis GZ, Blivis D, Liu W, et al. Early functional impairment of sensory-motor connectivity in a mouse model of spinal muscular atrophy. *Neuron* 2011;69:453-67

85. Liu H, Lu J, Chen H, et al. Spinal muscular atrophy patient-derived motor neurons exhibit hyperexcitability. *Sci Rep* 2015;5:12189

86. Sahashi K, Ling KK, Hua Y, et al. Pathological impact of SMN2 mis-splicing in adult SMA mice. *EMBO Mol Med* 2013;5:1586-601

87. Issa AN, Zhan WZ, Sieck GC, et al. Neuregulin-1 at synapses on phrenic motoneurons. *J Comp Neurol* 2010;518:4213-25

88. Casanovas A, Salvany S, Lahoz V, et al. Neuregulin 1-ErbB module in C-bouton synapses on somatic motor neurons: molecular compartmentation and response to peripheral nerve injury. *Sci Rep* 2017;7:40155

89. Casas C, Herrando-Grabulosa M, Manzano R, et al. Early presymptomatic cholinergic dysfunction in a murine model of amyotrophic lateral sclerosis. *Brain Behav* 2013;3:145-58

90. Mavlyutov TA, Epstein ML, Liu P, et al. Development of the sigma-1 receptor in C-terminals of motoneurons and colocalization with the N,N'-dimethyltryptamine forming enzyme, indole-N-methyl transferase. *Neuroscience* 2012;206:60-8

91. Murray LM, Comley LH, Thomson D, et al. Selective vulnerability of motor neurons and dissociation of pre- and post-synaptic pathology at the neuromuscular junction in mouse models of spinal muscular atrophy. *Hum Mol Genet* 2008;17:949-62

92. Kong L, Wang X, Choe DW, et al. Impaired synaptic vesicle release and immaturity of neuromuscular junctions in spinal muscular atrophy mice. *J Neurosci* 2009;29:842-51

93. Lee YI, Mikesh M, Smith I, et al. Muscles in a mouse model of spinal muscular atrophy show profound defects in neuromuscular development even in the absence of

failure in neuromuscular transmission or loss of motor neurons. *Dev Biol* 2011;356:432-44

94. Ling KK, Gibbs RM, Feng Z, et al. Severe neuromuscular denervation of clinically relevant muscles in a mouse model of spinal muscular atrophy. *Hum Mol Genet* 2012;21:185-95

95. Kariya S, Park GH, Maeno-Hikichi Y, et al. Reduced SMN protein impairs maturation of the neuromuscular junctions in mouse models of spinal muscular atrophy. *Hum Mol Genet* 2008;17:2552-69

96. Murray LM, Beauvais A, Bhanot K, et al. Defects in neuromuscular junction remodelling in the Smn(2B/-) mouse model of spinal muscular atrophy. *Neurobiol Dis* 2013;49:57-67

97. Perry VH, Nicoll JA, Holmes C. Microglia in neurodegenerative disease. *Nat Rev Neurol* 2010;6:193-201

98. Cherry JD, Olschowka JA, O'Banion MK. Neuroinflammation and M2 microglia: the good, the bad, and the inflamed. *J Neuroinflammation* 2014;11:98

99. Tang Y, Le W. Differential roles of M1 and M2 microglia in neurodegenerative diseases. *Mol Neurobiol* 2016;53:1181-94

100. Kigerl KA, Gensel JC, Ankeny DP, et al. Identification of Two Distinct Macrophage Subsets with Divergent Effects Causing either Neurotoxicity or Regeneration in the Injured Mouse Spinal Cord. *Journal of Neuroscience* 2009;29:13435-44

101. Franco R, Fernández-Suárez D. Alternatively activated microglia and macrophages in the central nervous system. *Prog Neurobiol* 2015;131:65-86

102. Kriz J, Nguyen MD, Julien JP. Minocycline slows disease progression in a mouse model of amyotrophic lateral sclerosis. *Neurobiol Dis* 2002;10:268-78

103. Kettenmann H, Kirchhoff F, Verkhratsky A. Microglia: new roles for the synaptic stripper. *Neuron* 2013;77:10-8

104. Zhang Y, Lv X, Bai Y, et al. Involvement of sigma-1 receptor in astrocyte activation induced by methamphetamine via up-regulation of its own expression. *J Neuroinflammation* 2015;12:29

105. Zhang XJ, Liu LL, Jiang SX, et al. Activation of the sigma receptor 1 suppresses NMDA responses in rat retinal ganglion cells. *Neuroscience* 2011;177:12-22

106. Witzemann V. Development of the neuromuscular junction. *Cell Tissue Res* 2006;326:263-71

107. Mavlyutov TA, Guo LW, Epstein ML, et al. Role of the Sigma-1 receptor in Amyotrophic Lateral Sclerosis (ALS). *J Pharmacol Sci* 2015;127:10-6

108. Saxena S, Roselli F, Singh K, et al. Neuroprotection through excitability and mTOR required in ALS motoneurons to delay disease and extend survival. *Neuron* 2013;80:80-96

109. Bernard-Marissal N, Medard JJ, Azzedine H, et al. Dysfunction in endoplasmic reticulum-mitochondria crosstalk underlies SIGMAR1 loss of function mediated motor neuron degeneration. *Brain* 2015;138:875-90

110. Prause J, Goswami A, Katona I, et al. Altered localization, abnormal modification and loss of function of Sigma receptor-1 in amyotrophic lateral sclerosis. *Hum Mol Genet* 2013;22:1581-600

111. Martina M, Turcotte ME, Halman S, et al. The sigma-1 receptor modulates NMDA receptor synaptic transmission and plasticity via SK channels in rat hippocampus. *J Physiol* 2007;578:143-57

112. Kinoshita M, Matsuoka Y, Suzuki T, et al. Sigma-1 receptor alters the kinetics of Kv1.3 voltage gated potassium channels but not the sensitivity to receptor ligands. *Brain Res* 2012;1452:1-9

113. Fletcher EV, Simon CM, Pagiazitis JG, et al. Reduced sensory synaptic excitation impairs motor neuron function via Kv2.1 in spinal muscular atrophy. *Nat Neurosci* 2017;20:905-16

114. Gurney M, Pu H, Chiu A, et al. Motor neuron degeneration in mice that express a human Cu,Zn superoxide dismutase mutation. *Science* 1994;264:1772-5

115. Moser JM, Bigini P, Schmitt-John T. The wobbler mouse, an ALS animal model. *Mol Genet Genomics* 2013;288:207-29

116. Nguyen L, Lucke-Wold BP, Mookerjee SA, et al. Role of sigma-1 receptors in neurodegenerative diseases. *J Pharmacol Sci* 2015;127:17-29

117. Mancuso R, Navarro X. Sigma-1 Receptor in Motoneuron Disease. *Adv Exp Med Biol* 2017;964:235-54

118. Philips T, Robberecht W. Neuroinflammation in amyotrophic lateral sclerosis: role of glial activation in motor neuron disease. *The Lancet Neurology* 2011;10:253-63

119. Evans MC, Couch Y, Sibson N, et al. Inflammation and neurovascular changes in amyotrophic lateral sclerosis. *Mol Cell Neurosci* 2013;53:34-41

120. McGivern JV, Patitucci TN, Nord JA, et al. Spinal muscular atrophy astrocytes exhibit abnormal calcium regulation and reduced growth factor production. *Glia* 2013;61:1418-28

121. Liddelow SA, Barres BA. Reactive Astrocytes: Production, Function, and Therapeutic Potential. *Immunity* 2017;46:957-67

122. Blinzinger K, Kreutzberg G. Displacement of synaptic terminals from regenerating motoneurons by microglial cells. *Z Zellforsch Mikrosk Anat* 1968;85:145-57

123. Chung WS, Clarke LE, Wang GX, et al. Astrocytes mediate synapse elimination through MEGF10 and MERTK pathways. *Nature* 2013;504:394-400

124. Eroglu C, Barres BA. Regulation of synaptic connectivity by glia. *Nature* 2010;468:223-31

125. Martinez TL, Kong L, Wang X, et al. Survival motor neuron protein in motor neurons determines synaptic integrity in spinal muscular atrophy. *J Neurosci* 2012;32:8703-15

126. Thirumalai V, Behrend RM, Birineni S, et al. Preservation of VGLUT1 synapses on ventral calbindin-immunoreactive interneurons and normal locomotor function in a mouse model of spinal muscular atrophy. *J Neurophysiol* 2013;109:702-10

127. Hao le T, Duy PQ, Jontes JD, et al. Motoneuron development influences dorsal root ganglia survival and Schwann cell development in a vertebrate model of spinal muscular atrophy. *Hum Mol Genet* 2015;24:346-60

128. Zhang Z, Pinto AM, Wan L, et al. Dysregulation of synaptogenesis genes antecedes motor neuron pathology in spinal muscular atrophy. *Proc Natl Acad Sci U S A* 2013;110:19348-53

129. Yamada J, Hayashi Y, Jinno S, et al. Reduced synaptic activity precedes synaptic stripping in vagal motoneurons after axotomy. *Glia* 2008;56:1448-62

130. Gekker G, Hu S, Sheng WS, et al. Cocaine-induced HIV-1 expression in microglia involves sigma-1 receptors and transforming growth factor-beta1. *Int Immunopharmacol* 2006;6:1029-33

131. Ruscher K, Inacio AR, Valind K, et al. Effects of the sigma-1 receptor agonist 1-(3,4-dimethoxyphenethyl)-4-(3-phenylpropyl)-piperazine dihydro-chloride on inflammation after stroke. *PLoS One* 2012;7:e45118

132. Hall AA, Herrera Y, Ajmo CT, Jr., et al. Sigma receptors suppress multiple aspects of microglial activation. *Glia* 2009;57:744-54

133. Behensky AA, Yasny IE, Shuster AM, et al. Stimulation of sigma receptors with afobazole blocks activation of microglia and reduces toxicity caused by amyloid-beta25-35. *J Pharmacol Exp Ther* 2013;347:458-67

134. Bourrié B, Bribes E, De Nys N, et al. SSR125329A, a high affinity sigma receptor ligand with potent anti-inflammatory properties. *Eur J Pharmacol* 2002;456:123-31

135. Ajmo CT, Vernon DOL, Collier L, et al. Sigma receptor activation reduces infarct size at 24 hours after permanent middle cerebral artery occlusion in rats. *Current Neurovascular Research* 2006;3:89-98

136. Prezzavento O, Campisi A, Parenti C, et al. Synthesis and resolution of cis-(+/-)-methyl (1R,2S/1S,2R)-2-[(4-hydroxy-4-phenylpiperidin-1-yl)methyl]-1-(4-methylphenyl)cycl opropanecarboxylate [(+/-)-PPCC)]: new sigma receptor ligands with neuroprotective effect. *J Med Chem* 2010;53:5881-5

137. Arumugam S, Garcera A, Soler RM, et al. Smn-deficiency increases the intrinsic excitability of motoneurons. *Front Cell Neurosci* 2017;11:269

138. McGovern VL, Iyer CC, Arnold WD, et al. SMN expression is required in motor neurons to rescue electrophysiological deficits in the SMNDelta7 mouse model of SMA. *Hum Mol Genet* 2015;24:5524-41

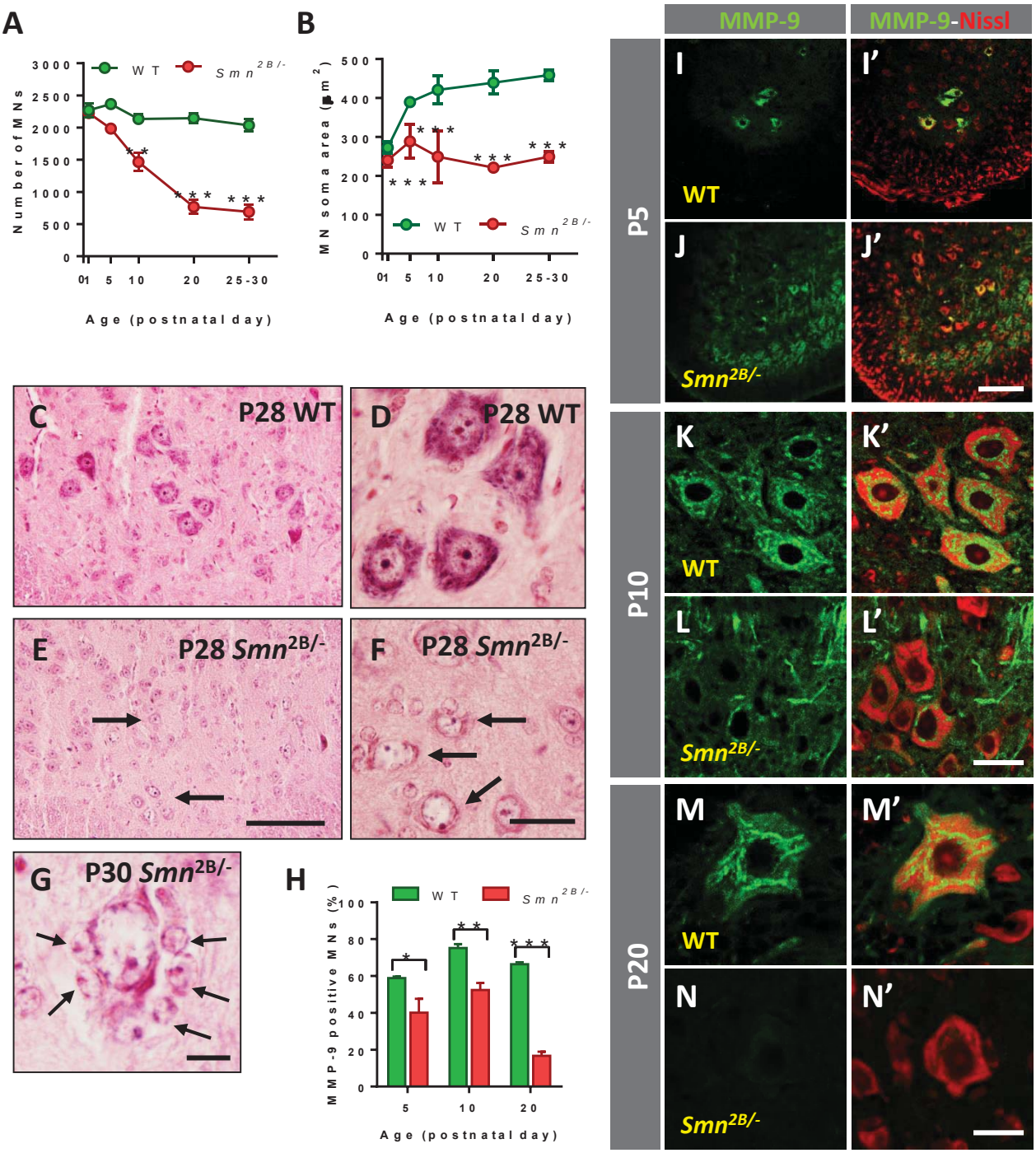

Figure 1

Figure 2

Click here to download Figure Fig_2.pptx

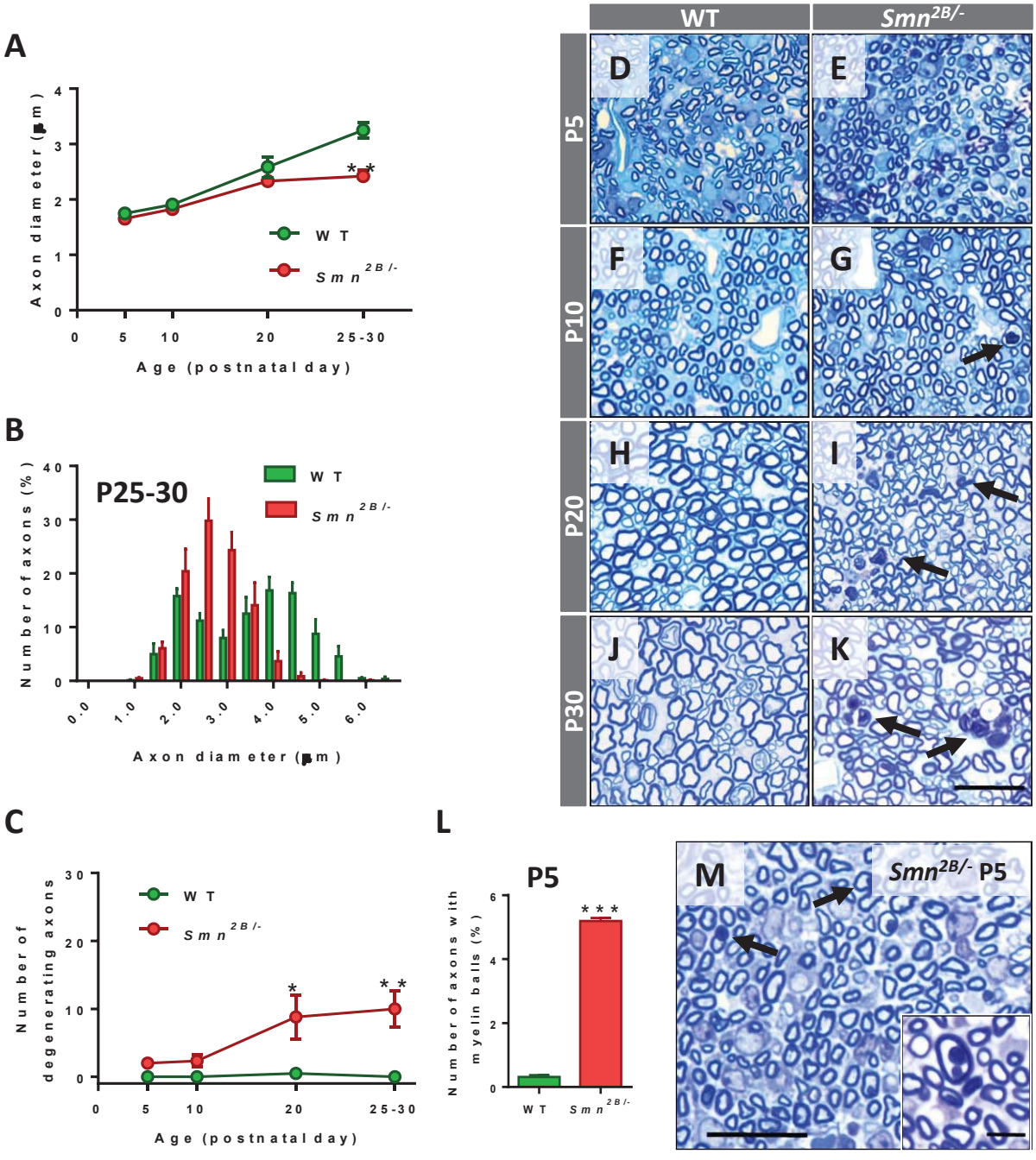

Figure 2

Figure 3

Click here to download Figure Fig_3.pptx

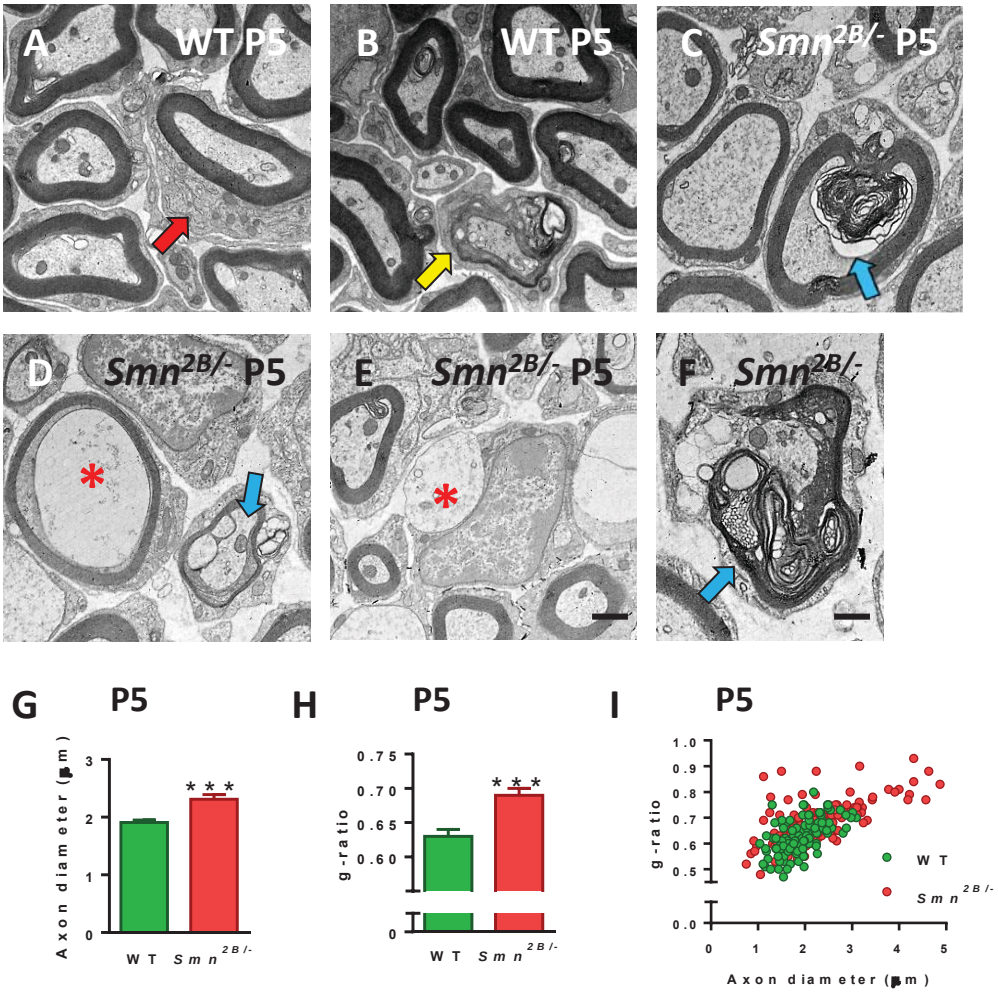

Figure 3

Click here to download Figure Fig_4.pptx

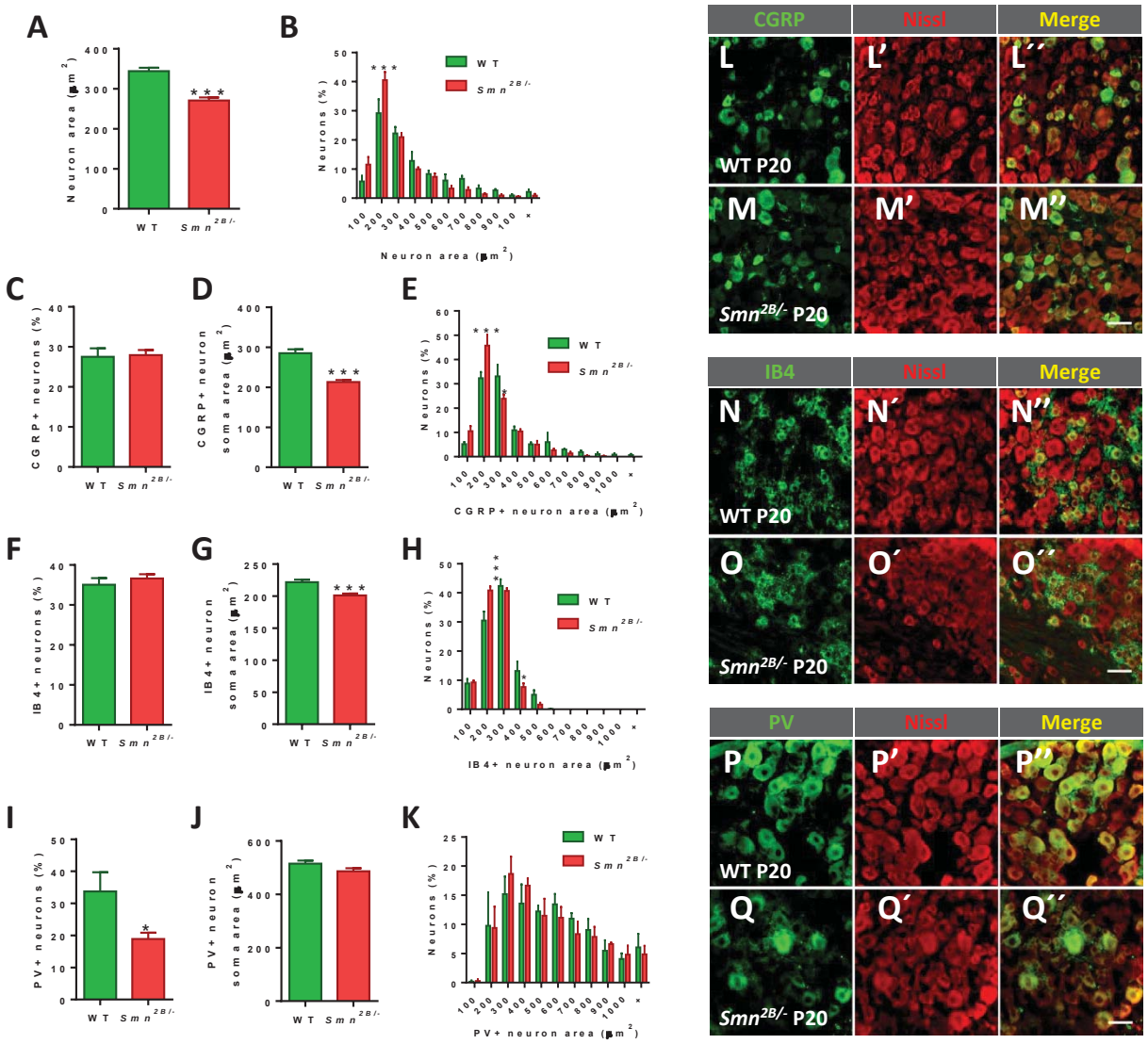

Figure 4

Figure 5

Click here to download Figure Fig_5.pptx

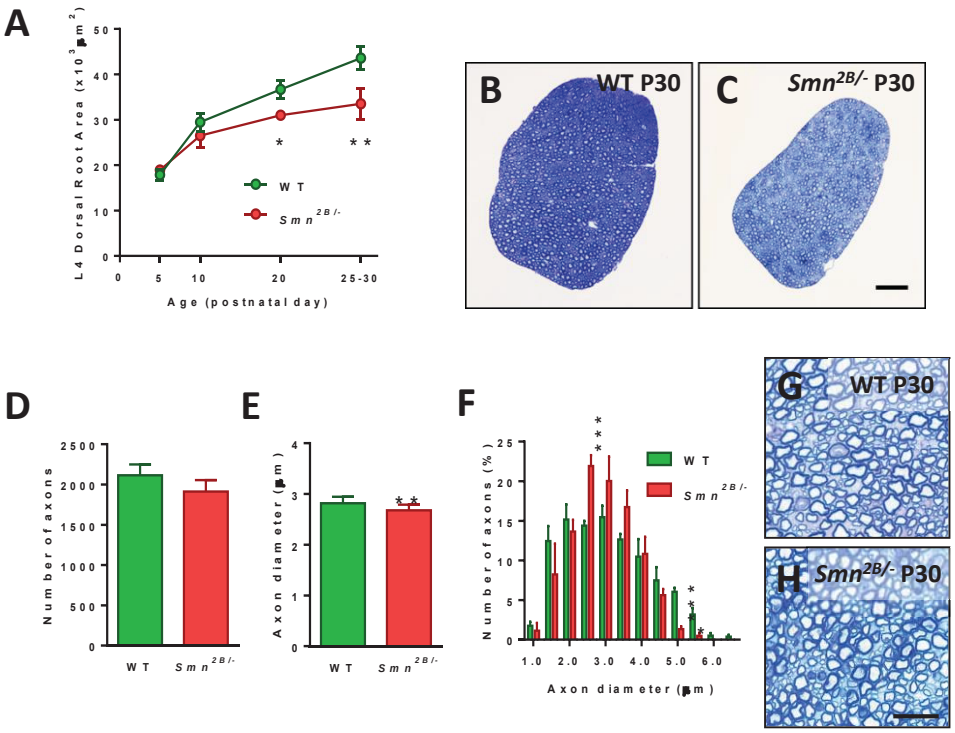

Figure 5

Figure 6

Click here to download Figure Fig_6.pptx

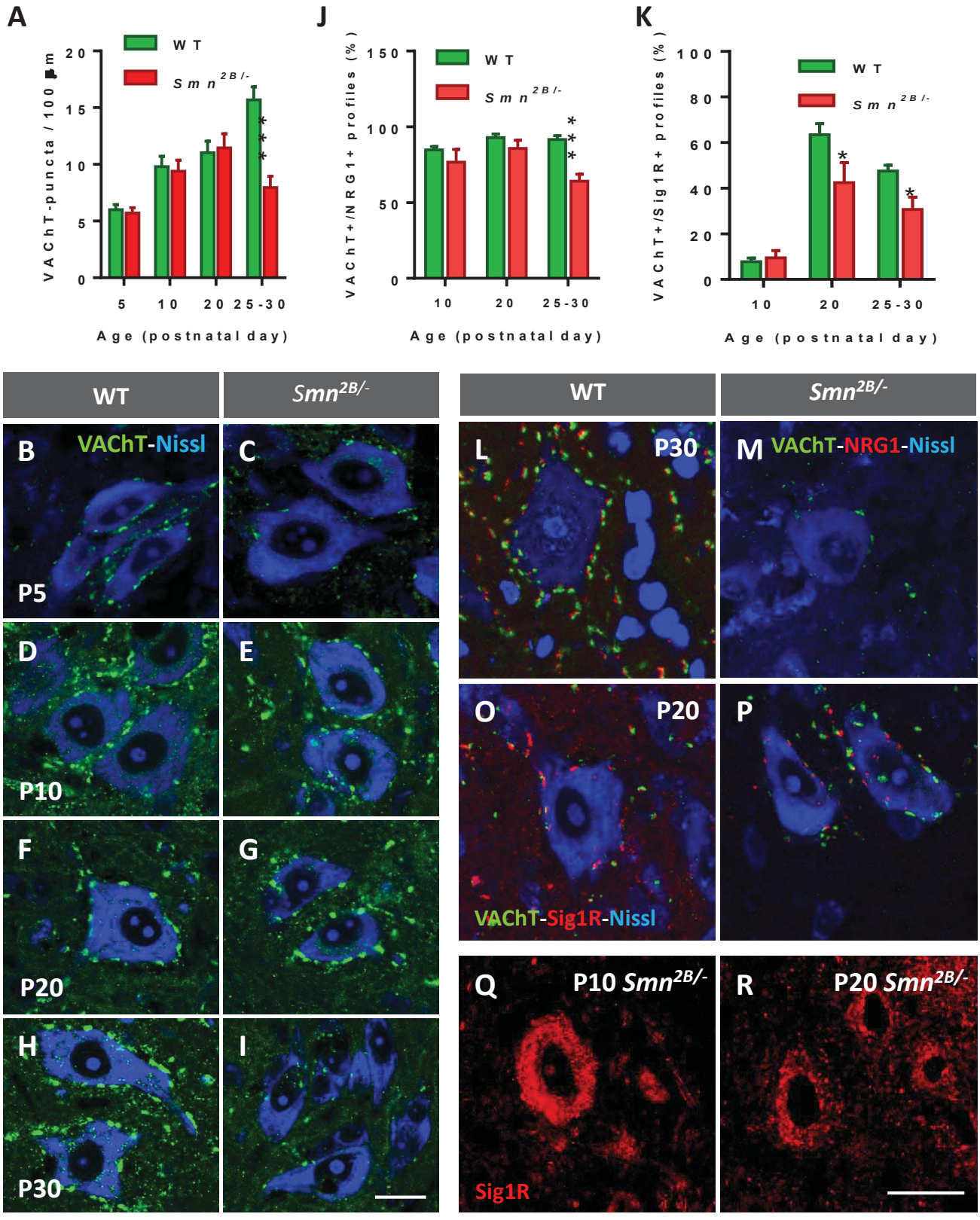

Figure 6

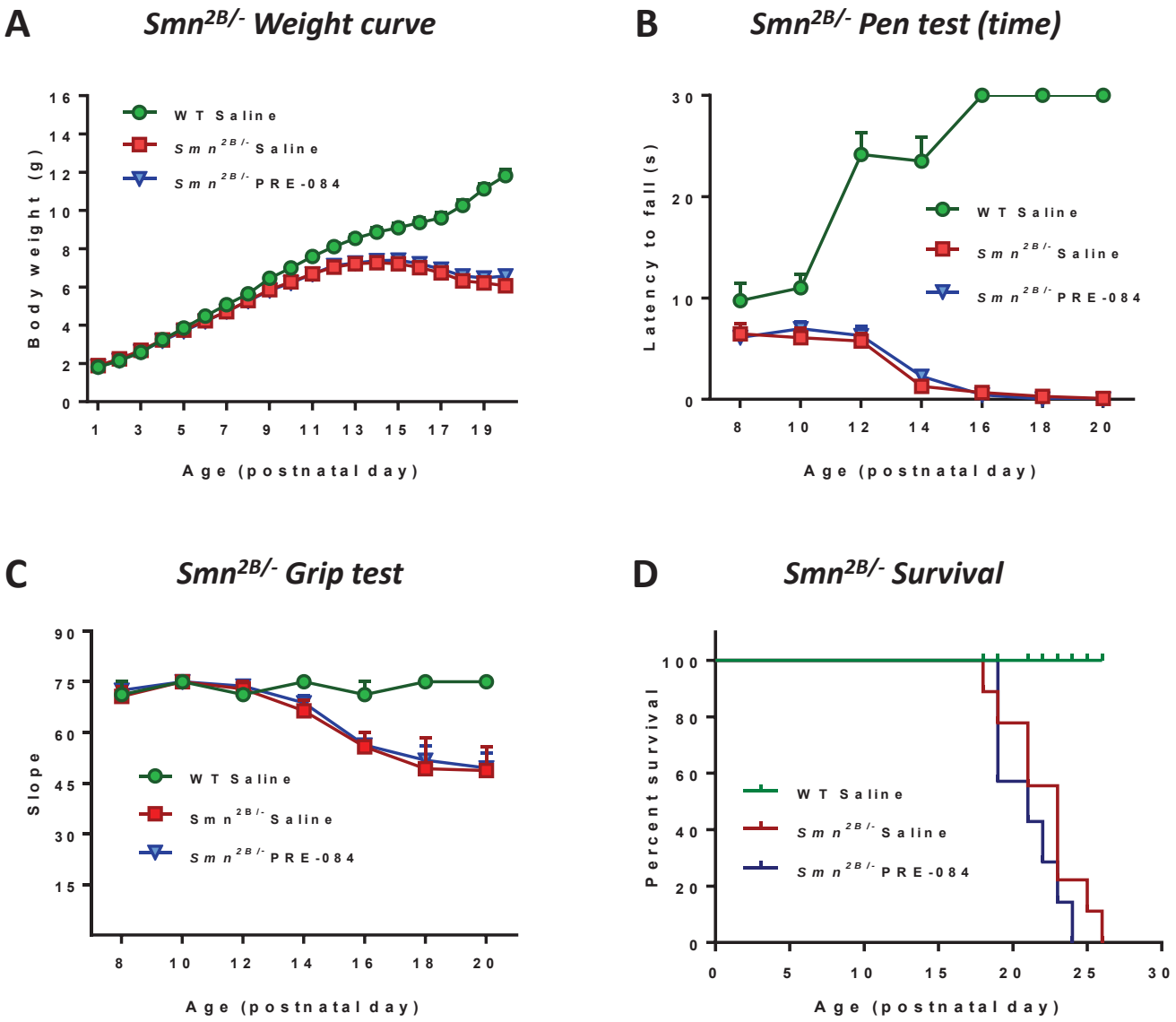

Figure 7

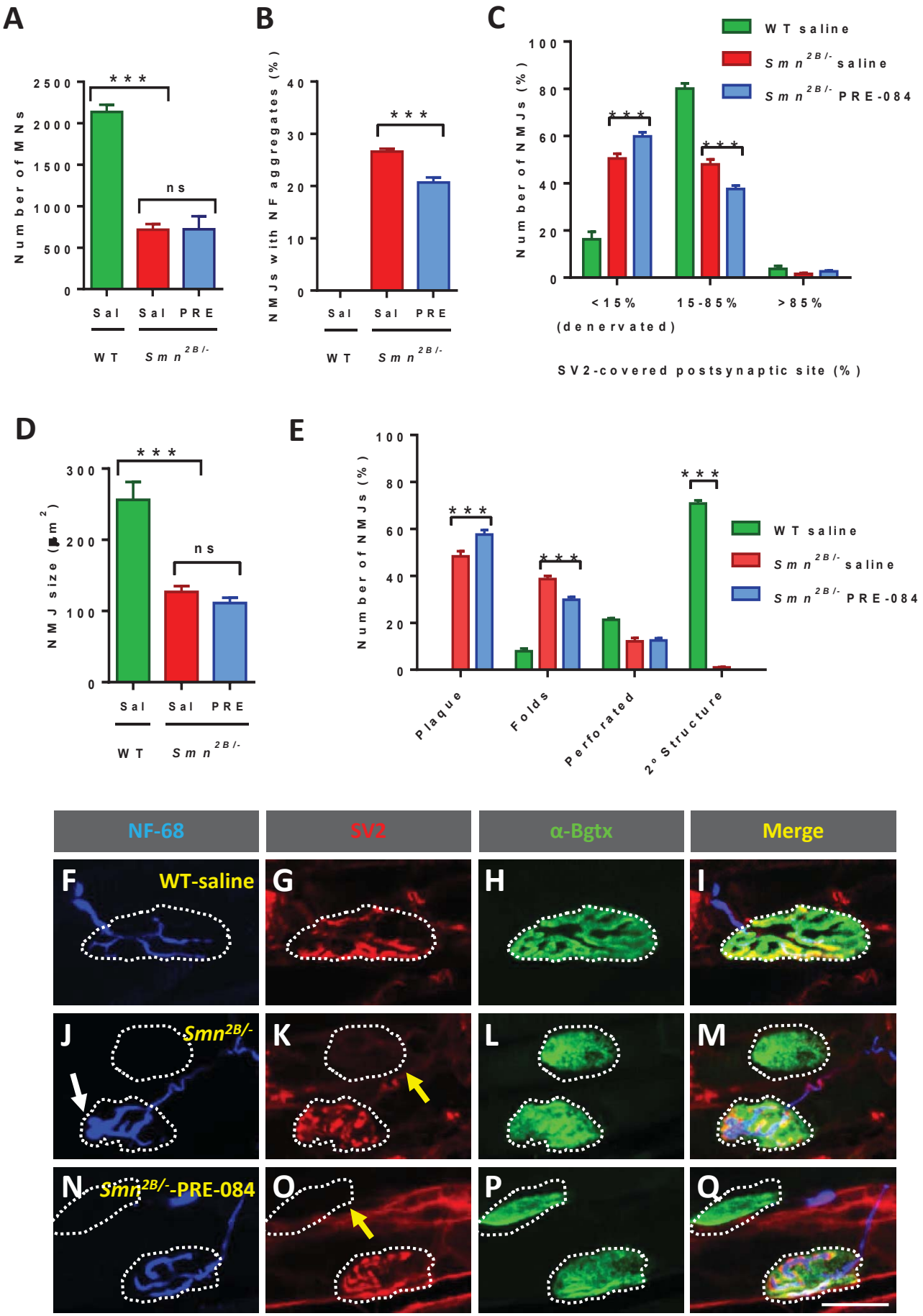

Figure 8

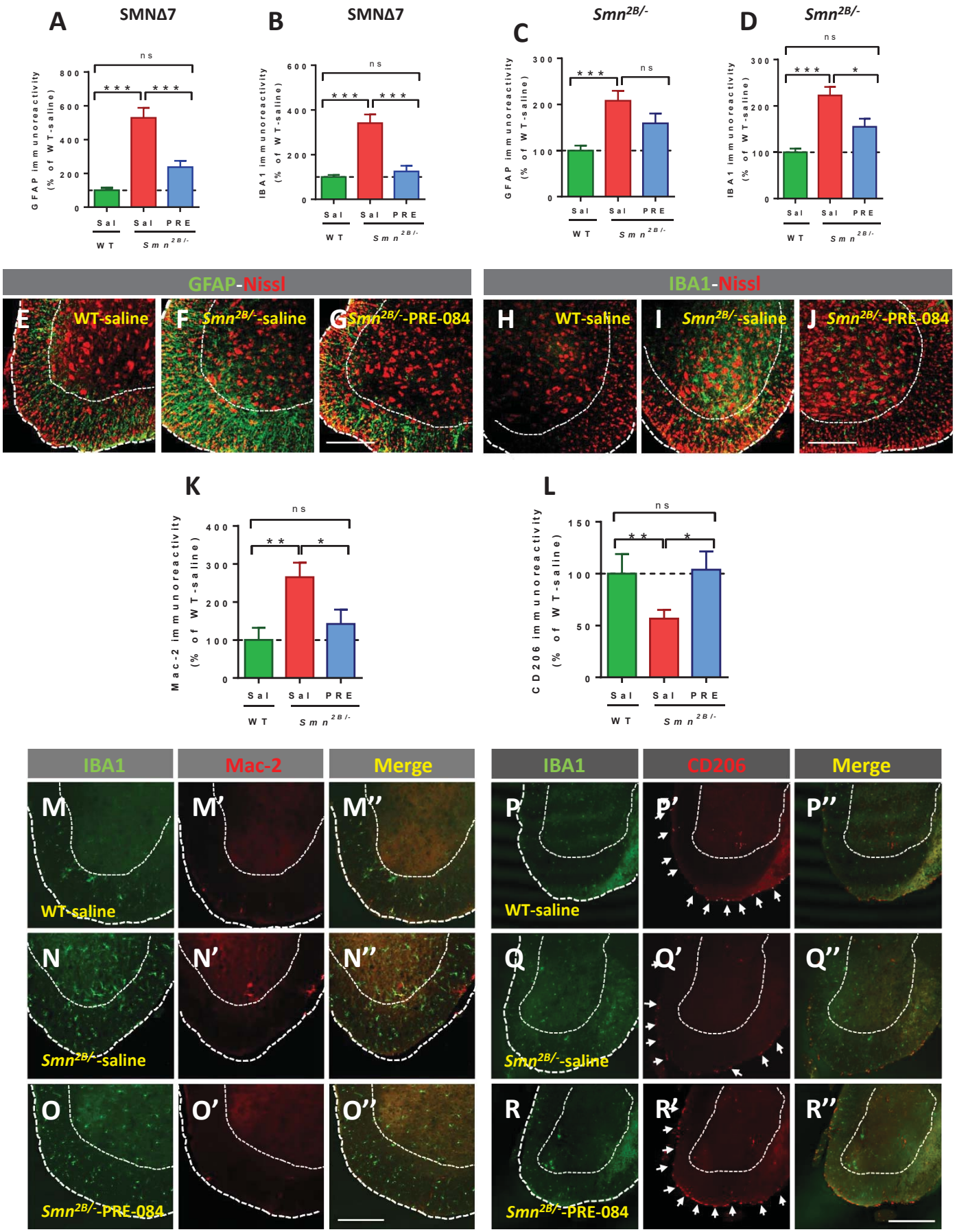

Figure 9

Figure 10

Click here to download Figure Fig_10.pptx

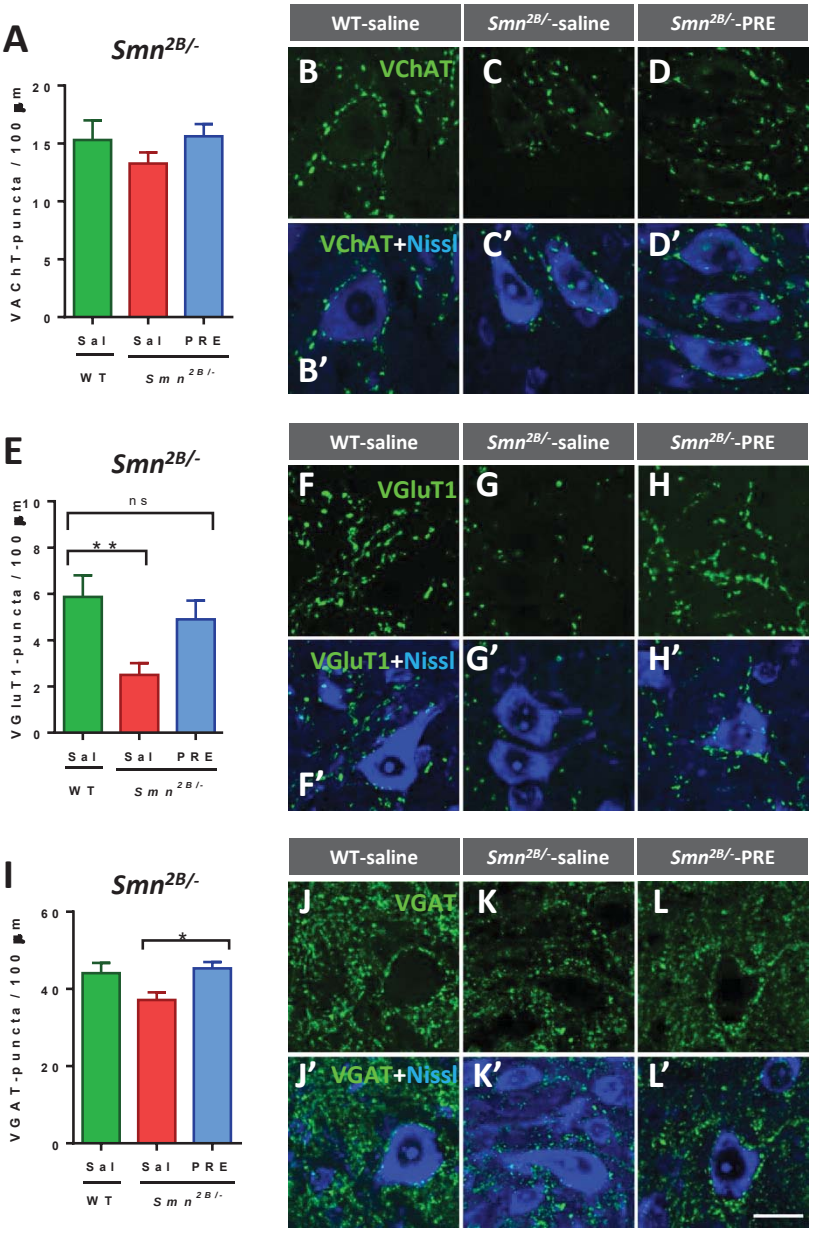

Figure 10

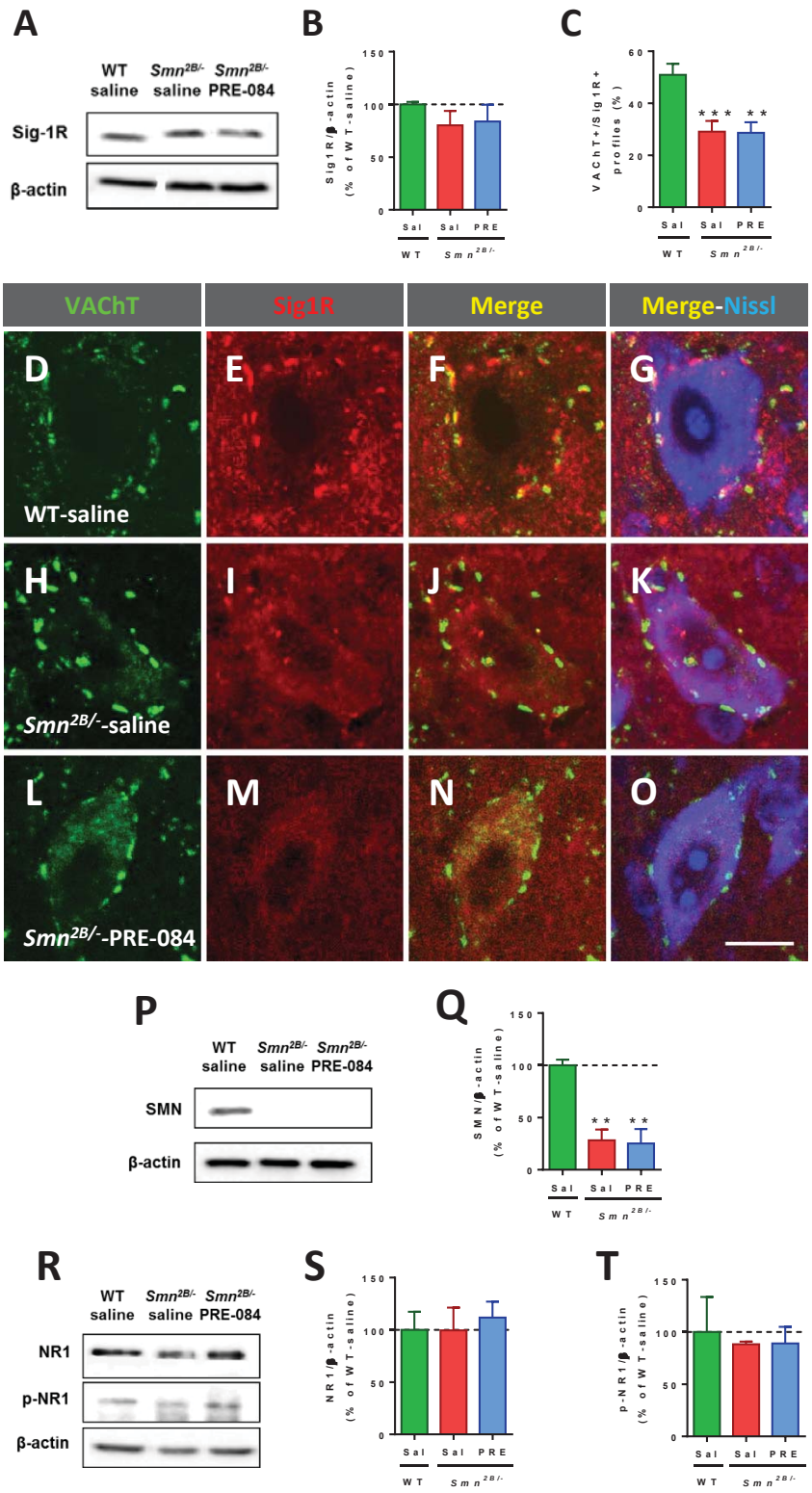

Figure 11